Single-molecule fluorescence of internalised biomolecules in live bacteria

Anne Plochowietz

A thesis submitted in partial fulfilment of the requirements for the degree of Master of Science by Research at the University of Oxford

University College

University of Oxford

Michaelmas Term 2012

Disclaimer

I hereby declare that the work in this thesis is that of the candidate alone, except where indicated in the text, and as described below.

- The microscope setups were designed and built by Dr. Ludovic Le Reste, Dr. Johannes Hohlbein, Dr. Ling Chin Hwang, Stephan Uphoff and Justin Pinkney.
- Hidden Markov Modelling analysis was implemented by Kristofer Gryte.
- The localisation and tracking software was developed by Dr. Seamus Holden and Stephan Uphoff.
- Initial experiments were performed under the guidance of Dr. Robert Crawford.
- The experiment on T7 RNA polymerase internalisation and expression of Emerald GFP in live bacteria was performed by Dr. Louise Aigrain.

Anne Plochowietz
November 2012

SINGLE-MOLECULE FLUORESCENCE OF INTERNALISED BIOMOLECULES IN LIVE BACTERIA

Anne Plochowietz, University College
(Biological Physics Research Group, Department of Physics)

Thesis submitted for the degree of Master of Science by Research
at the University of Oxford, Michaelmas Term 2012.

ABSTRACT

In the last two decades emerging single-molecule fluorescence tools have been developed and adapted to study individual molecules *in vitro* under various conditions and to reveal biochemical and cellular processes in live cells with high precision.
Single-molecule investigations *in vivo* rely mainly on fluorescent protein (FP) fusions with low quantum yield and photostability. Methods to introduce organic-labelled fluorescent molecules into cells have been achieved for mammalian cells via microinjection (not possible with bacteria) and are limited in throughput.
We have developed a physical transfection method for delivering organic-fluorophore labelled biomolecules into live bacteria for single-molecule studies. We internalised labelled dsDNA and proteins (up to 100 kDa) with high efficiency whilst maintaining cell viability. I was able to count the number of internalised molecules through photobleaching analysis. From this analysis, I was able to tune the concentration of internalised material from high concentrations compatible with localisation-based super-resolution imaging to lower concentrations compatible with single-molecule observation. Using localisation and tracking algorithms I followed the diffusion of individual molecules for up to 10 s and monitored the tracking paths within the cellular cytoplasm.
This method allows us to observe molecules for up to 10 minutes (FPs $\sim$ 5 s) under continuous illumination opening a new time regime to study biological processes. Our approaches are general and widely applicable to different microorganisms using biomolecules labelled with organic fluorophores already available for *in vitro* experiments.

Acknowledgements

I am very grateful to all the people who helped me with my work within the last year.

I would like to thank Dr. Achillefs Kapanidis for the opportunity to work on this project in the lab and his constant support on my behalf.

I really enjoy(ed) working in the team 'in vivo' – many thanks for the excellent cooperation, fruitful discussions and friendship go to Dr. Louise Aigrain, Dr. Robert Crawford and Marko Sustarsic. Special thanks to Dr. Robert Crawford and Dr. Ludovic Le Reste who helped me to get started in the lab.

For bringing each morning joy and colour into the office and for her friendship, Alexandra Tomescu.

For editorial assistance with the thesis I want to thank Dr. Louise Aigrain, Dr. Robert Crawford and Kristofer Gryte.

Thanks to all "Kapanidians" for their warm welcome and the great atmosphere in the group.

This work would not have been possible without the financial support of the German Academic Exchange Service. I am very thankful to Prof. Jörg Enderlein, Prof. Arnulf Quadt and Prof. Frank Kirchhoff for their help and support with the application at the University of Oxford.

Der größte Dank gilt meiner Familie und meinem Freund, Felix Geyer, für deren Rückhalt und deren Unterstützung in meinem Studium.

Anne Plochowietz, Oxford, November 2012

Published work arising from the MSc(Res)

R Crawford*, JP Torella*, L Aigrain*, **A Plochowietz***, K Gryte, S Uphoff, AN Kapanidis. Long-lived, ultrasensitive intracellular fluorescence using electroporated biomolecules. *Nature Methods*. *equal contribution. In preparation.

Conference Presentations

L Aigrain and **A Plochowietz**: Single-molecule FRET measurements in bacterial cells. Poster-prize at the 12th European Light Microscopy Initiative (ELMI) in Leuven, Belgium.

A Plochowietz: Long-lived *in vivo* single-molecule fluorescence using electroporated biomolecules. Delivered talk at the 18th International Picoquant Workshop on “Single Molecule Spectroscopy and Ultrasensitive Analysis in the Life Sciences” in Berlin, Germany.

Contents

List of abbreviations

Alexa647	commercial name of a cyanine dye
ATTO647N	commercial name of an oxazine dye
BSA	bovine serum albumin
Cy3B	cyanine 3B
DNA	deoxyribonucleic acid
DNA PolI	*E.coli* DNA polymerase I
dsDNA	double-stranded DNA
EDTA	ethylendiaminetetraacetic acid
EmGFP	Emerald green fluorescent protein
EP	electroporation
FL	fluorescence light (image)
FOV	field of view
FP	fluorescent protein
FRET	Förster resonance energy transfer
GFP	green fluorescent protein
GUI	graphical user interface
HMM	Hidden Markov Modelling
IPTG	isopropyl β-D-1-thiogalactopyranoside
M9	minimum media
MSD	mean-squared displacement
NHS	N-hydroxysuccimide
PAGE	polyacrylamide gel electrophoresis
PBS	phosphate buffered saline
PSF	point spread function

SOC	super optimal broth with catabolite repression
ssDNA	single-stranded DNA
T7RNAP	T7 RNA polymerase
TIRF	total internal reflection fluorescence (microscopy)
WL	white-light (image)

Chapter 1

Introduction

The ability to probe single biological molecules *in vitro* and in live cells has been developed over the last two decades (1, 2). Single-molecule fluorescence microscopy is an important tool to reveal fundamental biological processes such as membrane processes, activity of central dogma enzymes and processes involved in gene regulation with unprecedented precision (3).

Single-molecule fluorescence studies report the behaviour of *individual* molecules giving direct access to molecular heterogeneities and allow real-time observation of state transitions or conformational dynamics that are inaccessible to ensemble measurements (4). For example, kinetics studies of binding and dissociation of transcription factors at the single-molecule level were carried out to study the regulation of gene expression (5). Recent studies have shown that single transcription factor binding events are capable of profoundly altering cellular phenotypes (6). Furthermore, single-molecule Förster resonance energy transfer (FRET) studies can measure conformational changes at the biologically relevant size scale (with a resolution of $\sim 0.5\,\mathrm{nm}$ in the 2 - $10\,\mathrm{nm}$ distance range). Applying single-molecule FRET, mechanistic details by which nucleic acids and proteins fold were studied (7).

Since native biomolecules are generally not optically detectable at the single-molecule

level a fluorescent probe can be attached to the biomolecule. Fluorescent proteins (FP) and organic fluorophores are mainly used for single-molecule fluorescence microscopy studies (8).

However, single-molecule fluorescence and FRET studies are often limited to *in vitro* settings, due to the difficulty of introducing the labelled biomolecule of interest into living cells. While *in vitro* experiments allow control over experimental variables, the behaviour of particular systems may differ inside the cell; physiological concentrations of enzymes and substrates, competitive molecular interactions and macromolecular crowding might alter the molecular behaviour (9).

In vivo single-molecule fluorescence dependent on FP fusion with the protein of interest was observed in *Caulobacter* cells in 2004 (10) and in *E.coli* cells in 2006 (11). Fluorescent proteins fusions are used for instance to track changes in protein number, to observe the labelled protein's binding behaviour and to study gene expression. But FPs are limited by their low brightness and photostability, relatively large size of 2-4 nm compared to organic dyes. Moreover, the labelling with FP is restricted to the N- or C-terminus limiting their application in FRET assays.

Single-molecule FRET was reported in living cells in 2010 (12). In this study, proteins labelled with organic fluorophores were introduced via microinjection into *mammalian* cells. Due to the size of the injection needle ($\varnothing$ 5 µm), this internalisation method cannot be applied to bacteria (size of 1-3 µm) and is laborious when applied to several cells. Further, the laborious nature of the work prevented the adoption of the microinjection technique by other labs up to now.

A high throughput method to introduce biomolecules labelled with organic fluorophores into bacterial and eukaryotic cells is needed. Thus, single-molecule fluorescence and single-molecule FRET measurements can be carried out *in vivo* to observe biomolecules, proteins such as DNA processing proteins and transcription factors,

in the cellular environment with high spatial resolution. Thus, the molecules' diffusion behaviour, their localisation within the cell and their binding to cellular substructures could be studied with down to 20 nm precision (13) and intra-molecular dynamics can be observed with a resolution of ~ 0.5 nm.

Chapter organisation

In this work electroporation is presented as a high throughput internalisation method of biomolecules such as short DNA fragments and proteins labelled with organic fluorophores into living bacteria. High internalisation efficiencies of $>$80% for DNA and a high cell viability after electroporation were achieved (chapter 3). Using stepwise photobleaching studies and wide-field imaging, I showed that 1 to $\sim$ 1000 molecules can be internalised in a single cell (chapter 4). At the single-molecule level, I used long diffusion tracks to monitor diffusion paths and apparent diffusion coefficients within the cell. The fluorescence signal of a single molecule could be observed for up to $\sim$ 10 minutes under continuous illumination opening a new temporal regime for studying cellular processes (chapter 5). The performance of the internalisation method for single-molecule observation in live bacteria and further applications, e.g. *in vivo* FRET studies, are discussed in chapter 6.

Chapter 2

Concepts of *in vivo* single-molecule fluorescence

An individual fluorophore molecule was first directly detected in aqueous solution by Keller and co-workers in 1990 (14). Since then improvements in the photophysical properties of the fluorophores and the sensitivity of optical imaging techniques have allowed the probing of single fluorescent molecules *in vivo* (2).

I present the key concepts to study single-molecule fluorescence in live bacteria. The relevant photophysical processes are described by means of two fluorophores used in this work (Cy3B – cyanine dye, ATTO647N – oxazine dye). Furthermore, the 'host' of the *in vivo* studies, the bacterium *Escherichia coli*, is presented and methods to introduce labelled biomolecules into bacterial cells are described.

2.1 Photophysics

To optically detect individual biomolecules a fluorescent probe must be attached to the biomolecule. Single-molecule fluorescence studies rely on the information revealed by the fluorophore attached to the biomolecule such as the molecule's exis-

tence, position and movement. Thus, understanding the photophysical properties of the fluorophore is of immense importance to interpret single-molecule fluorescence observations.

2.1.1 Fluorescence

Generally, a fluorophore is a compound that absorbs energy of specific wavelength and emits energy at a different but equally specific wavelength. The spectrum of the emitted energy is a property of the fluorophore and might be affected by its chemical environment. The shift of the fluorescence emission band compared to the absorption band is caused due to radiationless deactivation processes such as vibrational relaxation via interaction with other solvent molecules (15). This phenomenon is called Stokes shift and is visualised in the absorption and emission spectra of the dyes Cy3B and ATTO647N in fig. 2.1. The spectrally red-shifted fluorescence emission can be efficiently detected using sensitive optical filtering.

Fluorophores exhibiting absorption in the visible spectrum are highly conjugate molecules, i.e. their carbon chain presents several double bonds separated by a single bond. In a conjugated chain, carbon atoms are linked by σ-bonds and are located in a common plane due to the σ-electrons wavefunction rotational symmetry. The conjugated system is embedded in a charge cloud of delocalised π-electrons characterised by a wavefunction having a node in the carbon chain plane. This π-bonds are weaker since the π-orbitals exhibit less overlap due to their parallel orientation. The delocalised π-electrons of these compounds can be excited by photons in the visible range of $390\,\mathrm{nm}$ to $750\,\mathrm{nm}$ and thus the fluorophore exhibit colour.

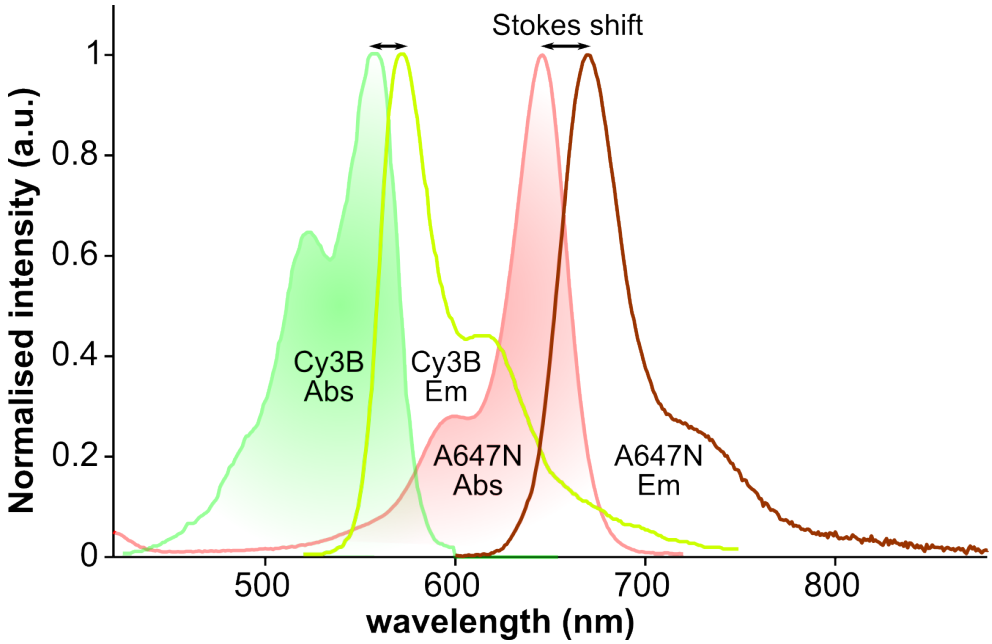

Figure 2.1: Absorption and emission spectra of fluorophore Cy3B (green) and ATTO647N (red). The emission spectra are red-shifted to the absorption spectra (Stokes shift) and thus allow separation of fluorescence emission via optical filtering.

2.1.2 Jablonski diagram

The possible transitions in the quantum states of a fluorophore can be visualised in the Jablonski diagram, fig. 2.2; a representation of the one dimensional energy landscape of the molecule's states. Quantum states can be separated into singlet states (paired electron spins) and triplet states (one set of unpaired electron spins). These states are superimposed with vibrational and rotational states. But the rotational quantum state ($\sim$ 0.001 eV) can be neglected at room temperature (thermal energy $\sim$ 0.025 eV).

The absorption of a photon with energy, $E = h\nu$[1], results in the excitation of the fluorophore from the lowest energetic state S_0 to the first excited state S_1. This process can be considered as instantaneous ($\leq$ 1 fs). Fluorophores excited in higher vibrational states of singlet states relax to the lowest vibrational state of S_1 with a rate

[1] ν: photon frequency, h: Planck constant

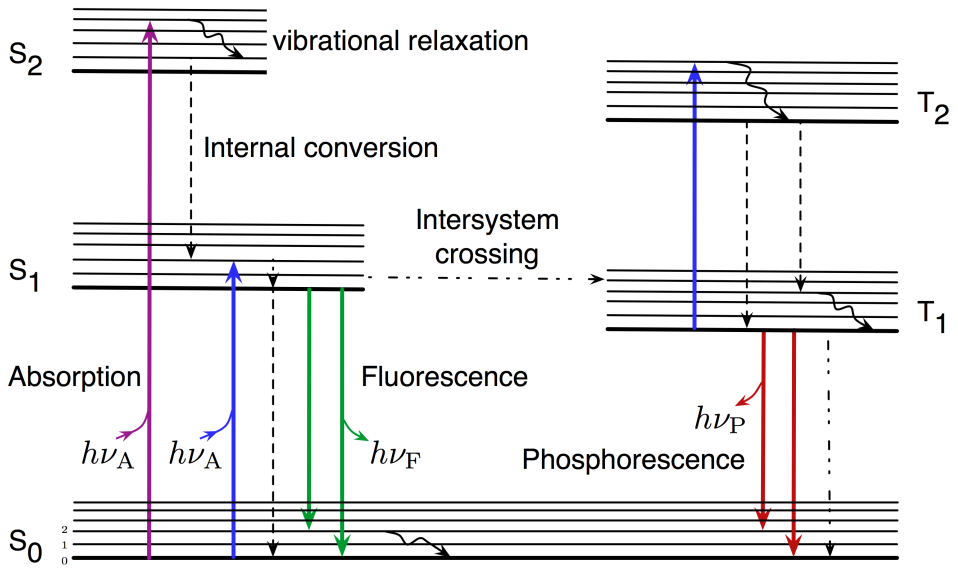

Figure 2.2: Jablonski diagram showing singlet states S_0, S_1 and S_2 and triplet states T_1 and T_2 with first 5 vibrational states. The state transitions are indicated with different kind of arrows.

constant of $k_{vib} \sim 10^{10}$-$10^{12}\,\mathrm{s}^{-1}$ via thermal collision with molecules (16).

Fluorophores in the first excited singlet state S_1 exhibit several phenomena

- radiative depopulation to ground state S_0 by spontaneous emission of a photon; fluorescence
- spin reversion by intersystem crossing into the first excited triplet state T_1
- radiationless internal conversion followed by vibrational relaxation to ground state S_0
- singlet-singlet absorption and subsequent ionisation of the fluorophore ($S_1 \rightarrow S_n$); one possible photobleaching pathway
- excitation to the higher singlet state S_2 followed by relaxation through internal conversion and vibrational relaxation

Although triplet-singlet state transitions are spin forbidden processes, the probability of intersystem crossing increases if there is a sufficient overlap of higher vibrational levels of the triplet state with lower vibrational levels of the singlet state. Triplet states exhibit very long lifetimes (up to 100 s whereas singlet state lifetimes are in the order of a few nanoseconds) and can only depopulate through vibrational relaxation followed by intersystem crossing or phosphorescence. Phosphorescence only occurs at low temperatures or in highly viscous media.

The various depopulation pathways of excited fluorophore states and their kinetic rates are listed in tab. 2.1.

Internal conversion	$S_n \rightarrow S_1, T_n \rightarrow T_1$	k_{ic}	$10^{10} - 10^{14}$ s^{-1}
Internal conversion	$S_1 \rightarrow S_0$	k_{ic}	$10^{6} - 10^{7}$ s^{-1}
Vibrational relaxation	$S_{1,\nu=n} \rightarrow S_{1,\nu=0}$	k_{vr}	$10^{10} - 10^{12}$ s^{-1}
Singlet-singlet absorption	$S_1 \rightarrow S_n$	k_{exc}	10^{15} s^{-1}
Triplet-triplet absorption	$T_1 \rightarrow T_n$	k_{exc}	10^{15} s^{-1}
Intersystem crossing	$S_1 \rightarrow T_1, S_n \rightarrow T_n, T_n \rightarrow S_n$	k_{isc}	$10^{5} - 10^{8}$ s^{-1}
Fluorescence	$S_1 \rightarrow S_0$	k_f	$10^{7} - 10^{9}$ s^{-1}
Phosphorescence	$T_1 \rightarrow S_0$	k_p	$10^{-2} - 10^{-3}$ s^{-1}

Table 2.1: List of possible depopulation pathways of excited fluorophores and transition rates (16).

The ideal fluorophore would cycle between the ground state and the first excited singlet state with two rates k_{exc} and k_f yielding a quantum yield of 100%, $\Phi_f = \frac{k_f}{k_f + k_{nf}} = 1$, if no non-fluorescent transitions occur ($k_{nf} = 0$). However, due to the presence of competing depopulation pathways of S_1 as described above, the fluorescent quantum yield never reaches 100%. Here, mainly intersystem crossing into long-lived triplet states decreases the probability to detect a fluorophore.

2.1.3 Photobleaching and blinking

Furthermore, irreversible photobleaching has to be considered when analysing the fluorophore's capability for fluorescence studies. Photobleaching is the loss of the dye's ability to emit fluorescence due to an irreversible reaction changing absorption and emission.

The pathways for photobleaching are complex and not fully understood and are dependent on the fluorophore, the environment of the fluorophore and the excitation settings (17, 18). In general, fluorophores in higher excited states especially triplet states with their long lifetime and slow rate of depopulation pathways are more reactive and thus more prone to photobleaching. The two major routes of photodestruction are via (i) photo-oxidation, the oxidation of a fluorophore in the triplet state by molecular oxygen and (ii) photoionisation, the formation of radical ions upon excitation to higher excited states (16).

In order to reduce photobleaching the time the fluorophore spends in long-lived triplet states or highly reactive excited states has to be minimised. Since molecular oxygen is directly (photo-oxidation) or indirectly (photoionisation) responsible for the photodestruction of fluorophores, enzymatic oxygen scavenging systems such as glucose oxidase-based systems have been developed (19, 20, 21).

However, molecular oxygen quenches the dye's triplet state resulting in a triplet state lifetime of a few microseconds in aqueous solution (22). Thus, oxygen removal results in an increase in the triplet state lifetime up to several milliseconds (23, 24, 25). Since triplet state blinking is not desired in many single-molecule applications an alternative triplet state quencher such as reducing compounds as β-mercaptoethanol (BME), β-mercaptoethylamine (MEA) and Trolox (26, 27, 28) were introduced. Furthermore, blinking can be caused by photoinduced electron transfer via collisions of the molecule with electron donors or acceptors and occur mainly in the long-lived

triplet state of the fluorophore. The resulting dark states can be ascribed to reduced or oxidised states of the fluorophore (redox blinking, (22)).

The addition of a combination of enzymatic oxygen scavenging system and triplet state quencher can effectively reduce blinking and photobleaching of fluorophores. The buffer systems can be easily controlled in *in vitro* settings but are rather difficult to introduce in *in vivo* studies. Note that in this study, no substances to control the photophysical properties of the dye *in vivo* were used and further studies on the dye's properties in live settings and their control have to be carried out.

2.2 *In vivo* fluorescent labels

Fluorophores for *in vivo* studies have to fulfill a list of requirements: (i) a high brightness ($\sim \Phi_f \cdot \epsilon$) to enhance single-molecule fluorescence detection and thus a high fluorescence quantum yield ($\Phi_f > 0.1$) and a high extinction coefficient ($\epsilon > 10^5 \text{cm}^{-1}\text{M}^{-1}$), (ii) a short fluorescence lifetime ($\tau_f < 5$ ns) to reduce the probability of non-fluorescence transitions, (iii) a large Stoke shift (15-30 nm) to be able to filter the excitation from the emission light, (iv) a high photostability and (v) a high biocompatibility (16).

The commercially available organic fluorophores used in this study (cyanine dyes: Cy3B and Alexa647, oxazine dye: ATTO647N) fulfill all these requirements. These dyes are widely used in sensitive single-molecule fluorescence studies (22). From these studies it is known that Alexa647 is less photostable compared to ATTO647N or Cy3B and exhibits blinking behaviour which is used in localisation-based super resolution studies (29, 30). The photophysical properties of the fluorophores are listed in tab. 2.2. For labelling of biomolecules such as DNAs and proteins, the dye must carry a functional group allowing covalently binding to free amino or thiol groups. NHS ester conjugated dyes are commonly used for *in vitro* amino group labelling; also

used in this work. The challenge is then to introduce the biomolecules labelled with organic fluorophores into the live cell. Such internalisaton methods are described in sec. 2.3

Fluorophore	λ_{exc} (nm)	λ_{fl} (nm)	τ_{fl} (ns)	ϵ (10^5 cm^{-1}M^{-1})	Φ_f
Cy3B	558	572	2.8	1.3	0.67
ATTO647N	644	669	3.5	1.5	0.65
Alexa647	650	668	1.0	2.7	0.33

Table 2.2: List of fluorophores and their photophysical properties used in this work; cyanine dye Cy3B (31), the oxazine dye ATTO647N (32, 16) and the cyanine dye Alexa647 (33, 34). Spectroscopic characteristics: λ_{exc} – absorption maximum, λ_{fl} – emission maximum, τ_{fl} – fluorescence lifetime, ϵ – extinction coefficient, Φ_f – quantum yield

One very elegant way of *in vivo* labelling commonly applied to proteins is to use genetically encoded fluorescent protein fusions. The DNA sequence of genetically encoded fluorescent proteins (FP) such as the green fluorescent protein (GFP) and its derivatives is placed next to the sequence coding for the protein of interest. During protein synthesis the protein of interest will be prepared as a GFP fusion protein (35). GFP was extracted from the bioluminescent jellyfish and consists of 238 amino acids forming a β-barrel cylindrical structure protecting the fluorophore in the middle. Fig. 2.3 shows the structure of GFP and two organic dyes used in this study. Next to the GFP wildtype a large variety of related proteins exist in the blue-cyan, yellowish and even red absorption spectrum (36).

However, fluorescent proteins are generally ten times less photostable and bright compared to organic dyes and exhibit complicated photophysics (blinking behaviour, etc.) (37, 38). FPs are mainly introduced at the protein termini and are large in size (note the different scalebars in fig. 2.3) which might influence expression and function of the protein of interest. Moreover, the strong autofluorescence of the cells especially in the blue and green spectral range challenge *in vivo* FP observation.

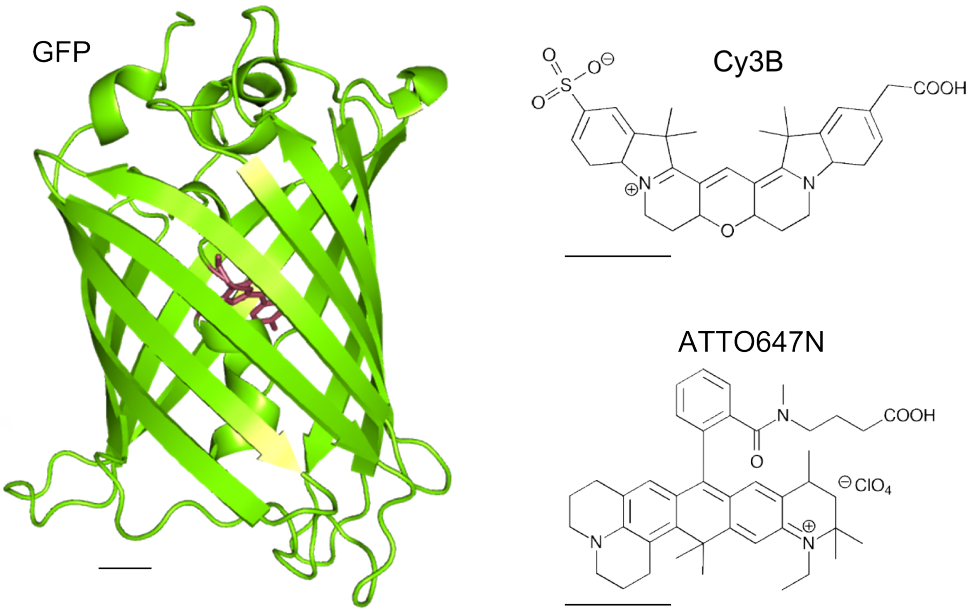

Figure 2.3: Schematic of the structure of the green fluorescence protein (GFP, pdb-file: 1GFL) and the organic dyes Cy3B (31) and ATTO647N (39, 40). Scale bar: 0.5 nm

The major problem of labelling the biomolecule with organic fluorophores inside the cell is to achieve site-specifically labelling which is especially required for single-molecule investigations and FRET assays. Several different protein fusion and tag-systems have been reported for *in vivo* labelling of proteins up to now (41, 42). However, these methods are highly specific and most of the tag-structures are large in size (SNAP-tags: $>$ 200 amino acids) and thus might introduce pertubations in protein expression and functionality. Furthermore, these labelling techniques need specific control mechanisms to ensure site-specific labelling of the protein.

To detecting specific sequences *in vivo* immunolabelling, for instance primary antibodies labelled with a fluorophore, are used. But even there, a high binding affinity of the antibody to the target is needed and distinguishing bound from unbound species is still not trivial. Hence, fluorescent probes highly specifically recognising their target and increasing fluorescence only upon molecular binding such as quenched DNA hairpin probes, molecular beacons or smart probes have been developed. A lot of

current research is done in this field to improve *in vivo* protein labelling.

2.3 Internalisation methods

In order to carry out fluorescence observation of a biomolecule of interest in live cells two ways can be pursued. First, the biomolecule could be labelled inside the cell. We already pointed out that here site-specifically labelling is difficult to achieve. Second, the already labelled biomolecules can be internalised into the cell for *in vivo* measurements. Standard *in vitro* labelling protocols can be easily applied but efficient and high throughput internalisation methods of the labelled biomolecules into the cells are needed.

Several internalisation methods of biomolecules into cells based on cell membrane permeabilisation have been studied. Endocytosis, detergent-mediated internalisation (43, 44), sonification (45) and microinjection (46, 47, 48, 12). However, these methods were mainly applied to large mammalian cells (size in the order of tens of micrometer) and are not applicable to bacterial cells (1-3 µm in size); for instance the needle used for microinjection needle has a diameter of about 5 µm. Moreover, microinjection can only be applied to one cell at a time and thus high throughput measurements are not possible.

In this work, electroporation (49) is used to introduce organic labelled biomolecules in bacterial cells. In the 1980s electroporation was developed in molecular biology, to transform or transfect prokaryotic and eukaryotic cells with plasmids or short DNA fragments (50, 51). During electroporation the cell membrane is permeabilised by exposing the low ionic cell suspension to the discharge of a high voltage electric field. The cell membrane gets rearranged by the high voltage electric field forming aqueous pores (reversible process). Biomolecules can enter the cell through this

transient pores. Thus, the conductance of the cell suspension increases leading to the exponential decay of the electric field (52).

Electroporation is performed by the discharge of a capacitor in a resistor-capacitor (RC) circuit over the low ionic cell suspension, fig. 2.4. Before electroporation, 'switch 1' is closed and the capacitor is charged. Then, 'switch 1' is opened and 'switch 2' is closed leading to the discharge of the high voltage electric field ($V_0 \sim 20\,\mathrm{kV/cm}$ with time constant[2] $\tau \sim 5$ ms, inset fig. 2.4) over the cell suspension in the electroporation cuvette. After electroporation, the cell suspension is recovered in a rich medium to reseal the membrane pores and prevent cell membrane lysis. The amplitude of the applied electric field V_0 and the time constant τ are important parameters that can be varied to optimise the internalisation process (53).

2.4 *Escherichia coli*

The bacteria *Escherichia coli* is a prokaryotic organism; i.e. it has no compartment like the cell nucleus to house its DNA. The genetic material is stored in the nucleoid, circular double-stranded DNA in the cytoplasm. The structural organisation of the gram-negative bacterium is shown in fig. 2.5; the cell interior exhibits no further structure.

E.coli are rod-shaped cells in the order of 1 to 3 µm and can be found in gut of humans or vertebrates. The bacteria *Escherichia coli* is a well-studied model organism. It is a laboratory favourite system, since the cells are easily to grow in nutrient broth. *E.coli* reproduce quite rapidly (20 min per generation in rich medium) and the cells show a high variety in their biochemical capabilities and adapt rapidly to chemical conditions (55). The basic genetic mechanisms (DNA replication, transcription and

[2]The time constant τ is dependent on the resistance of the circuit R and the capacitance of the capacitor C, $\tau = RC$.

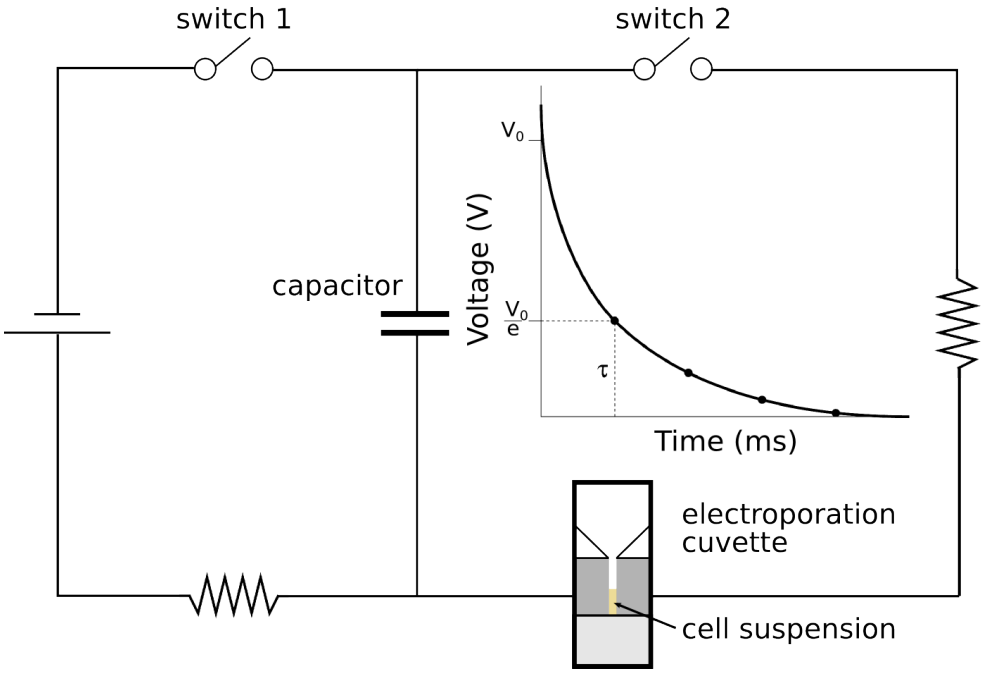

Figure 2.4: Schematic of electroporation process. The resistor-capacitor (RC) circuit presents the basic principle of an electroporator. First, the capacitor is charged ('switch 1' closed). A cuvette containing the low ionic strength cell suspension of labelled molecules and electrocompetent bacteria between two metal plates is placed into the right circuit ('switch 2' is still opened). For electroporation 'switch 1' is opened and 'switch 2' is closed. The capacitor is discharged across the cell suspension. The voltage decays exponentially with $\tau = RC = 5\,\text{ms}$ from the initial voltage of $V_0 = 1.8\,\text{kV}$. Electroporation is described to form transient pores within the cell membrane through which the labelled biomolecules can enter the cell.

translation) have turned out to be highly conserved throughout evolution. Thus, fundamental mechanism in life such as protein synthesis were learned from studies in *E.coli*.

To get an impression of the importance of this model system, the whole genome of the standard *E.coli* K-12 strain consisting of approximately 4.6 million nucleotide pairs was one of the first sequenced genomes in 1997 (56). The base pair sequence encodes for about 4300 different proteins.

In the single-molecule field processes were studied in live *E.coli*. For instance, flagella's function in motion and as a sensory organelle was extensively studied and the stepping behaviour of the flagella motor was revealed (57, 58). Furthermore, the spa-

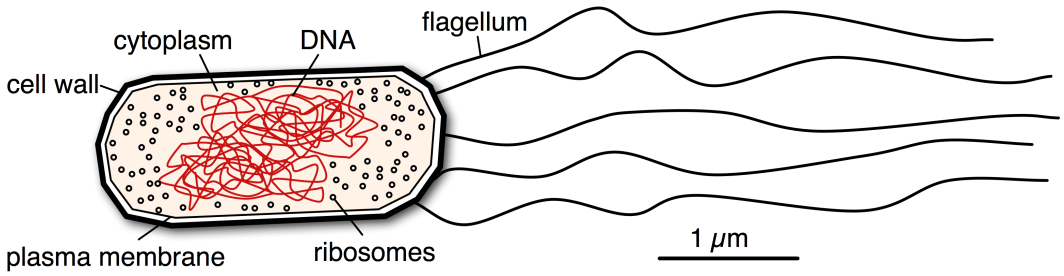

Figure 2.5: Schematic of E.coli representing the different components. The cell wall/'protective capsule' consists of the outer membrane, the periplasmic space and the pepticoglycan (54).

tial organisation of the replicating bacterial chromosome (59), gene expression (11) and individual transcription factor dynamics (5, 6, 60) were monitored in live bacteria. In this work, I present a method to internalise biomolecules labelled with organic fluorophores into bacteria and thus I hope to provide another avenue to study biological processes in live *E.coli*.

Chapter 3

Internalisation of biomolecules

Electroporation is presented as an efficient internalisation method of biomolecules labelled with organic fluorophores (DNA and protein) into live *E.coli*. The cell fluorescence signal and the cell viability after electroporation were studied. Furthermore, the internalisation of biomolecules into the cellular cytoplasm and their functionality were shown.

3.1 Internalisation of dsDNA standards

To internalise the dsDNA standards labelled with organic fluorophores into cells, electroporation was performed. Electroporation is commonly used on prokaryotic and eukaryotic cells for transfection with plasmids or short DNA fragments (51).

First, the 45 bp dsDNA standards were labelled with selected NHS-tagged organic fluorophores such as Cy3B, ATTO647N or Alexa647 and stored in a low-salt annealing buffer. For the DNA sequences and the labelling protocol see sec. A.1.

In this case, 10 pmol of dsDNA standards labelled with Cy3B or ATTO647N were added to 20 µL of electrocompetent cells (ElectroMAX^{TM} DH5α-E^{TM} Competent Cells, Invitrogen/ Life technologies, Carlsbad, California, USA) and incubated for 10 min on

ice. The suspension of cells and labelled biomolecules was then transfered into a pre-chilled electroporation cuvette (0.1 cm gap, Bio-Rad, Hercules, California, USA) and placed into an electroporator (Micropulser, Bio-Rad). The cell suspension was exposed to the discharge of a high-voltage electric field (initial electric field of 18 kV/cm, time constant of 5 ms, sec. A.2.1) forming transcient pores in the cell membrane through which the dsDNA standards could enter the cell (53). Immediately after electroporation, 500 µL of a rich medium (super optimal broth with catabolite repression, SOC) was added to the cell suspension and the cells were let to recover by shaking for 20 min at 37 °C. After recovery, the cells were harvested by centrifugation at 3300 g for 1 min at 4 °C and washed 5 times with 500 µL phosphate buffered saline (PBS). Cells were finally resuspended in 100-200 µL PBS and stored on ice before pipetted onto a 1% agarose-M9 pad, fig. 3.1 A.

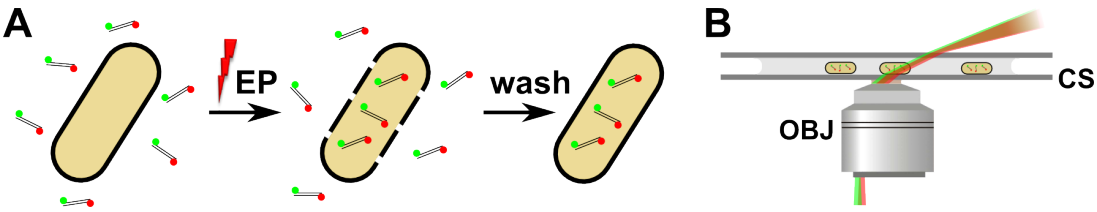

Figure 3.1: Internalisation of organic fluorophore labelled biomolecules into bacteria using electroporation and monitored by fluorescence microscopy. **A**. Schematic illustrating internalisation method. Fluorescent biomolecules were incubated with electrocompetent cells prior to electroporation (EP). Cells were then recovered, washed and placed on agarose pads for observation. **B**. Observation of loaded cells using objective-based near-TIRF or wide-field illumination. (OBJ – objective; CS – coverslip).

The cells were imaged on the agarose pad using an inverted microscope in wide-field mode or in objective-based near-total internal reflection fluorescence (near-TIRF) mode, fig. 3.1 B. In near-TIRF mode the sample is illuminated by a highly inclined laser beam (61). Near-TIRF illumination provides a high illumination intensity and a high signal-to-noise ratio whilst illuminating more than half of the cell. Up to $\sim$ 40 cells could be imaged per field of view at a time.

Bacterial cells electroporated with 10 pmol dsDNA Cy3B or dsDNA ATTO647N were imaged in wide-field mode, fig. 3.2. The majority of cells ($>$ 70%, quantification as described in sec. 4.3) appeared significantly more fluorescent than non-electroporated cells (negative control). The dark negative control proved that fluorescently labelled DNA molecules do not stick to the outside of the membrane. The imaged cells showed a wide distribution in fluorescent brightness correlating to the number of internalised biomolecules. A qualitative analysis of the fluorescent images showed bright cells that were heavily loaded (yellow box), dimmer cells only containing a few molecules (white box) and cells that were not loaded at all (cyan box). This clearly showed that dsDNA standards of $\sim$ 15 nm in size can be efficiently internalised into *E.coli* using electroporation.

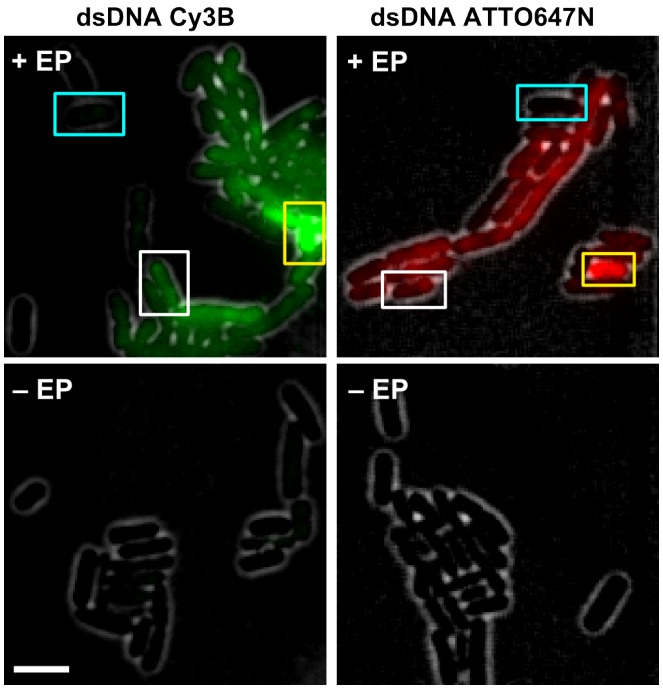

Figure 3.2: Proof of concept: internalisation of dsDNA into *E.coli* bacteria using electroporation. Overlay of inverted white-light and fluorescence images of cells loaded with 10 pmol dsDNA labelled with a green (Cy3B, left) or red (ATTO647N, right) fluorophore. + EP (top) indicates electroporated cells showing fluorescence inside cell boundary. A large variation in brightness can be observed: bright cells (yellow box), dimmer cells (white box) and dark cells (cyan box). – EP (bottom) indicates non-electroporated cells showing negligible fluorescence. Scale bar: 3 µm

Furthermore, I added different amounts of labelled dsDNA before electroporation and included dsDNA labelled with Alexa647 in the internalisation study. Cells electroporated with different amounts of dsDNA and fluorophores with different structure and emission wavelength showed again a good uptake and a wide spread in cell intensities, fig. 3.3. From the representative field of views of the different samples (10 pmol and 100 pmol dsDNA Cy3B and ATTO647N, 5 pmol dsDNA Alexa647) I could already observe that the more DNA was added before electroporation the brighter the cells were. A quantitative analysis of actual numbers of internalised biomolecules per cell is presented in chapter 4.

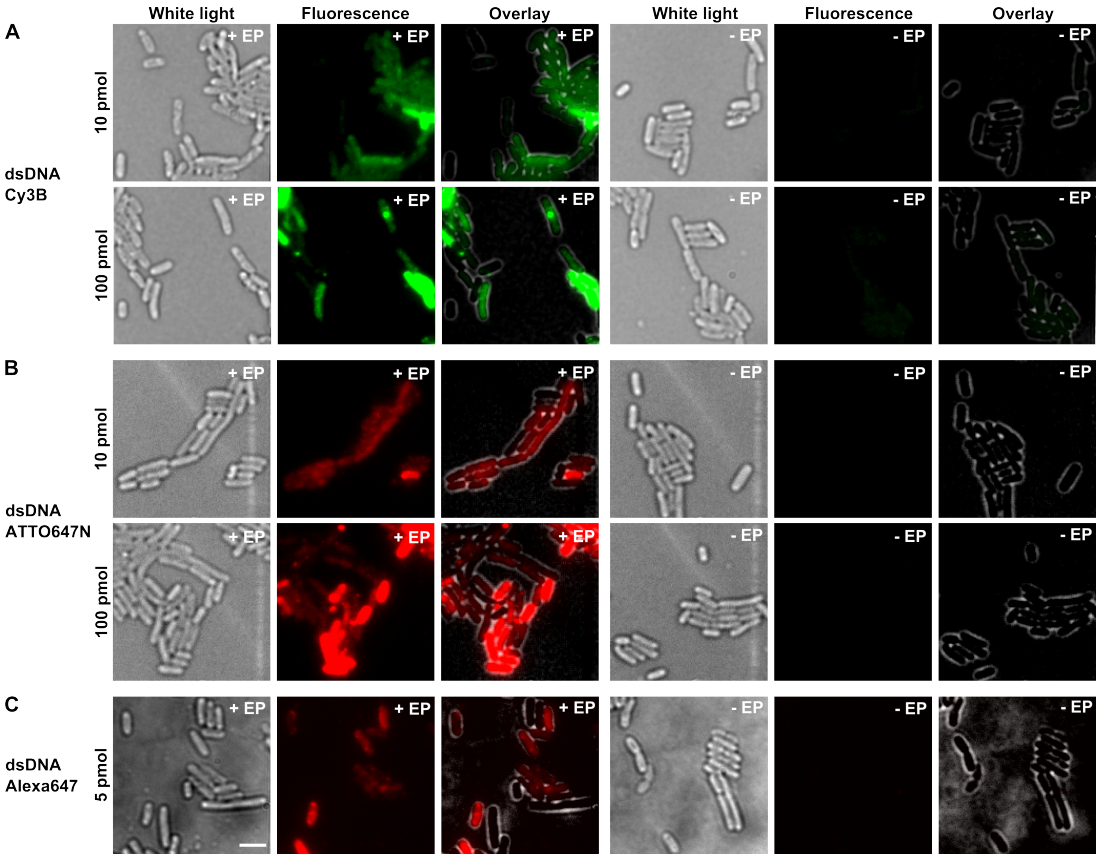

Figure 3.3: Internalisation of different amounts of dsDNA added before electroporation and labelled with different organic fluorophores into *E.coli*. White-light image, fluorescence image and overlay of inverted white-light and fluorescence image of cells loaded with dsDNA labelled with Cy3B (**A**), ATTO647N (**B**) and Alexa647 (**C**). + EP (left) indicates electroporated cells showing a wide distribution in brightness. – EP (right) indicates non-electroporated cells, the negative control. Scale bar: 3 µm

Electroporation was established as an efficient, high throughput internalisation method for a variety of dsDNA fragments labelled with different organic fluorophores. The cells showed a large variety in brightness suggesting a wide distribution in numbers of internalised fluorescent DNA molecules.

3.2 Viability check of cells

The growth and division of cells was used as an indicator for their viability after electroporation and fluorescent DNA uptake. Therefore, the cells were imaged over many generations on a 1% agarose-EZ rich defined medium pad in wide-field fluorescence imaging mode. The cells loaded with $100\,\mathrm{pmol}$ of dsDNA ATTO647N were monitored for more than 5 hours every $30\,\mathrm{min}$ for the first three hours. About each $90\,\mathrm{min}$ EZ rich defined medium was added to the channel system within the agarose pad to keep it wet. The sample preparation is described in sec. A.2.2.

Cell division was analysed for 362 cells. A representative selection of cells within the first hour is shown in fig. 3.4. About 50% of the cells were dividing with a division time of $\geq 30\,\mathrm{min}$ (green circles). The cells in the blue circle retain their shape, representing about 45% of the cells. Only less than 5% of the cells were compromised (red circle). Importantly, the division of the cells was independent from their loading (cells in green circles). Furthermore, the fluorescence signal distributed evenly between daughter cells and thus was preserved upon division (data not shown).

The majority of cells is not affected by electroporation and the uptake of dsDNA labelled with organic fluorophores. For more than $\sim$ 90% of the cells the cell physiology is not disturbed.

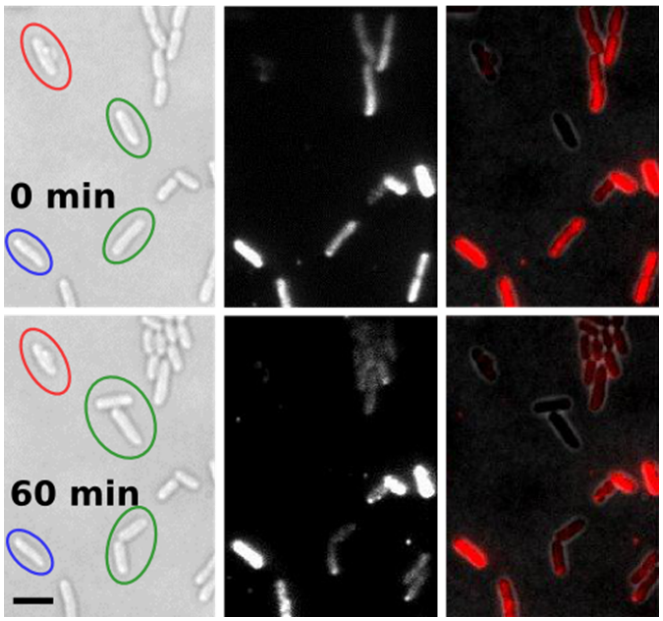

Figure 3.4: Cell viability after electroporation. White-light image (left), fluorescence image (middle) and overlay (right) of cells electroporated with 100 pmol dsDNA ATTO647N at 0 and 60 min after recovery. About 50% of the cells divide within 60 min (example: green circles), $\sim$ 45% do not show division (example: blue circle), and $<$ 5% are compromised (example: red circle). Cell viability is independent of cell loading. Scale bar: 3 µm

3.3 Internalisation of T7RNA polymerase and expression of Emerald GFP

To prove that the electroporated biomolecules were inside the cellular cytoplasm and functional, homemade DH5α electrocompetent cells were prepared. The bacterial cells were transfected with the pRSET-EmGFP (Invitrogen/ Life technologies, Carlsbad, California, USA) plasmid. This plasmid contains several important elements – a *lacI* gene which codes for the *lac* repressor protein, a *lac* operator which can block transcription, a T7 promotor which is specific to only T7RNA polymerase (not bacterial RNA polymerase) and an ampicillin resistance gene. Thus, only in presence of electroporated non-labelled T7RNA polymerase (T7RNAP, New England BioLabs Inc, Ipswich, Massachusetts, USA) in the bacterial cytoplasm, the Emerald Green

Fluorescent Protein (EmGFP) should be expressed inside the bacteria, yielding to a higher fluorescence signal compared to non-electroporated and empty cells containing only the plasmid. This would prove the activity of the electroporated protein and would give an estimate of the size of proteins that could be internalised.

Electroporation of 2 µL of T7RNAP (stock concentration of 1 µM) was performed with a modified protocol. The cells were recovered in 500 µL of SOC containing Isopropyl β-D-1-thiogalactopyranoside (IPTG, 2 mM final concentration) for about 1 h at 37 °C and imaged on a 1% agarose pad with EZ rich defined medium (Teknova, Hollister, California, USA). The cells were illuminated with blue laser light ($P(\lambda = 475\,\mathrm{nm}) = 0.5\,\mathrm{mW}$) with an exposure time of 100 ms in wide-field mode.

About 700 cells per sample were analysed using an automated segmentation routine, sec. A.4.1. The cell intensity normalised by the cell area was plotted in a histogram for each cell, fig. 3.5. The intensity distribution of empty cells containing the plasmid looked similar to the negative control. For the negative control, T7RNAP was added to the cell suspension and incubated in SOC containing IPTG for 1 h without electroporation. The electroporated cells showed a higher amount of bright cells (about 14 %) and less dim cells compared to the empty cells and the negative control (histogram bar highlighted with "$*$") giving good evidence of the expression of the fluorescent protein EmGFP.

We noticed that the homemade electrocompetent bacteria DH5α transfected with the plasmid encoding the EmGFP showed already relative high autofluorescence in the blue channel compared to the electrocompetent bacteria DH5α purchased from Invitrogen not containing the plasmid. This could be caused by the leak-expression of EmGFP through other RNA polymerases inside *E.coli*. Furthermore, the T7RNAP protein has a size of about 99 kDa which decreases the internalisation efficiency. Internalisation of proteins of this size like DNA polymerase I (103 kDa) showed already

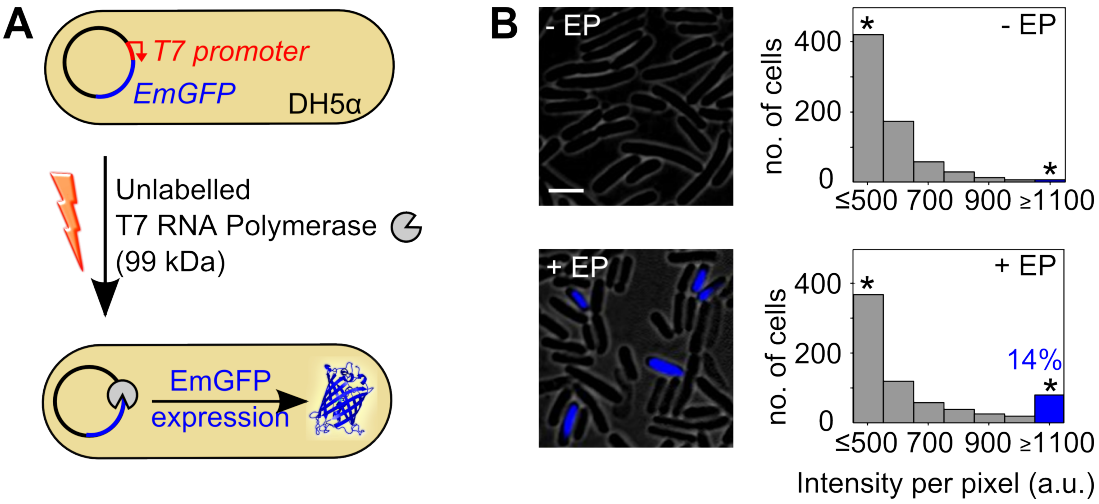

Figure 3.5: Internalisation of unlabelled T7RNA polymerase (T7RNAP, 99 kDa) into electrocompetent DH5α *E.coli* previously transformed with pRSET-EmGFP plasmid encoding Emerald GFP (EmGFP) under control of the *lac* operon T7 promoter. **A**. Schematic of the protein activity assay showing the internalisation of unlabelled T7RNAP and expression of EmGFP. **B** (left). Overlay of inverted white-light and fluorescence image of a representative field of view of non-electroporated cells (-EP) and electroporated cells (+EP). **B** (right). Histogram of cell-based fluorescence intensities for 700 cells per sample; cells incubated with T7RNAP without electroporation (-EP) and cells incubated with T7RNAP with electroporation (+EP). About 14% of the electroporated cells show higher fluorescence intensity than the negative control. Higher fluorescence indicates expression of EmGFP and therefore active internalised T7RNAP. Scale bar: 3 µm

a very low internalisation efficiency compared to proteins of about 60 kDa (data not shown, Crawford et al. in preparation (62)). Furthermore, the detection of a small number of FPs is challenging because of the high cellular autofluorescence background, so that we detected only cells in which several EmGFP molecules have been expressed. This explains, why the effect of T7RNAP internalisation and EmGFP expression ranges in the order of $\sim$ 15%.

The experiment gives good confidence that the internalised biomolecules are functional after electroporation and inside the bacterial cytoplasm. Moreover, it shows that biomolecules of up to 100 kDa can be internalised into living bacteria using electroporation.

Contributions

I performed and analysed all dsDNA internalisation experiments. Louise Aigrain and I carried out the cell viability experiment and Louise Aigrain analysed the cell division. The internalisation of T7RNAP was performed by Louise Aigrain and I provided a Matlab GUI for automated cell segmentation and fast cell-based fluorescence analysis, sec. A.4.1.

Chapter 4

Counting numbers of internalised biomolecules

The number of internalised biomolecules is an important characteristic of the electroporation method. It allows the evaluation of the amount of biomolecules to add before electroporation when studying internalised biomolecules at the single-molecule level (tracking and diffusion analysis) or on the cell-based level. Furthermore, knowing the order of magnitude of loaded biomolecules inside a cell is useful when studying for instance the impact of internalised transcription factors on gene regulation or the influence of loaded DNA polymerase I on DNA repair.

4.1 Photobleaching studies

To count the number of internalised biomolecules, single cell-based photobleaching studies were performed. Cells loaded with dsDNA ATTO647N were exposed to high laser power in wide-field mode ($P(\lambda = 638\,\mathrm{nm}) = 3\,\mathrm{mW}$, exposure time $100\,\mathrm{ms}$) until the fluorescence signal vanished. The fluorescence signal of an entire cell containing about 1 to 10 molecules decreases in quantised steps under con-

tinuous laser excitation. Each single step corresponds to a photobleaching event. Fig. 4.1 shows three typical time traces of the fluorescence decay (blue curve) and a fitted step function (red curve). The cells were segmented manually using a custom-written MATLAB script or automatically (with manual adjustment) by adapting the MATLAB implementation 'Schnitzcells' by the Elowitz lab (63) for white-light cell images, sec. A.4.1. Using a custom-written Matlab script, the overall cell intensity per cell area was calculated for each movie frame and subtracted by the cell background per cell area (obtained after the loaded fluorescent biomolecules and the cellular autofluorescence were completely bleached). Baseline-subtracted photobleaching time traces showing less than 10 quantised steps were fitted using Hidden Markov Modelling (HMM), sec. 4.2. The three fitted cell-based photobleaching time traces shown in fig. 4.1 represent the variety of observed cells. Cells only loaded with one active fluorophore at acquisition start showed a single photobleaching event, fig. 4.1 – top, whereas bleaching and blinking behaviour of the dye ATTO647N was observed in fig. 4.1 – middle. The bottom time trace, fig. 4.1 – bottom, shows approximately 8 steps corresponding to 8 molecules inside the bacteria.

Furthermore, the photobleaching analysis was used to evaluate the signal sensitivity of organic fluorophores inside bacteria and to estimate the intensity of a single fluorophore (single-molecule unitary intensity) by calculating the mean step height intensity. Previously, photobleaching studies were carried out to count individual molecules such as stators in bacterial flagellar motors (64) or to measure the stoichiometry of membrane protein complexes in live bacterial cells (65). The photobleaching time traces were filtered for instance using the edge-preserving non-linear Chung-Kennedy filter (66), the pairwise difference distribution function (PDDF) was calculated and the peak of the power spectrum of the PDDF was detected which corresponds to the single-molecule unitary intensity.

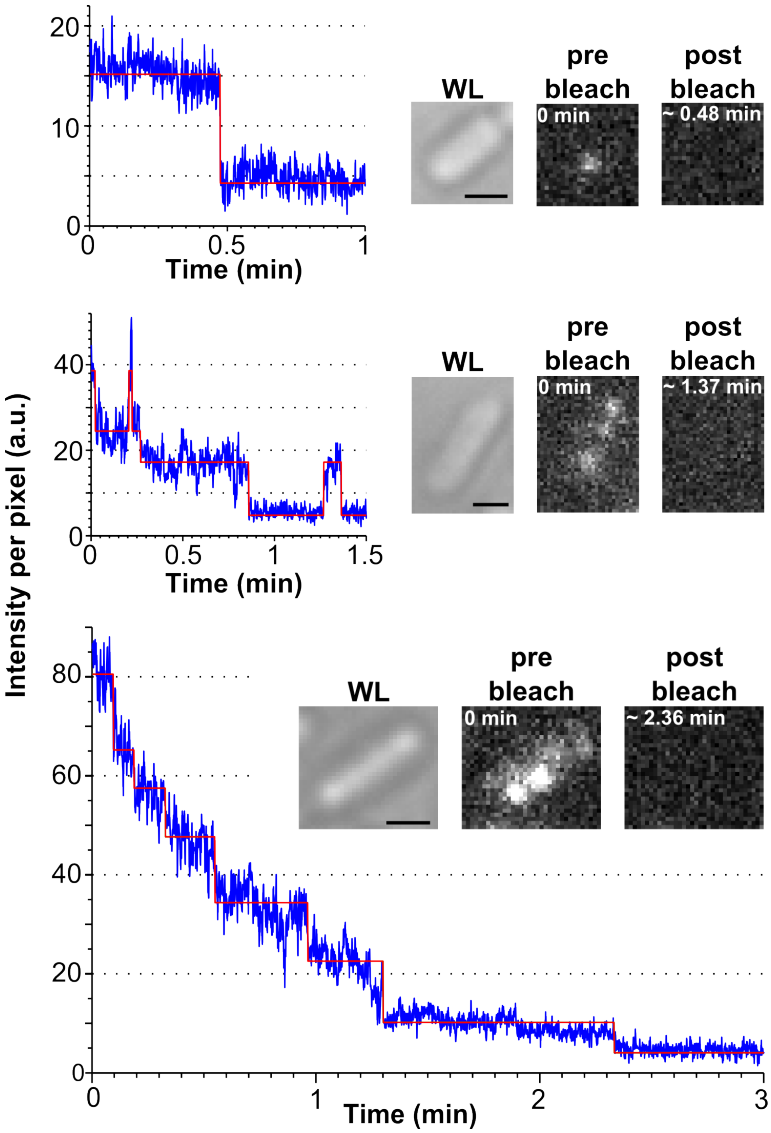

Figure 4.1: Cell-based photobleaching step analysis. Three examples of fluorescence decay time traces (blue: raw data; red: hidden markov model (HMM) fit). Top: Single step bleach event. Middle: Step analysis of cell containing $\sim$ 3 molecules showing bleaching and blinking behaviour of the dye ATTO647N. Bottom: Step analysis showing approximately 8 steps corresponding to 8 internalised single molecules. Inset: White-light image (WL) and fluorescence image (FL) of the cell at the start of acquisition and after photobleaching. Scale bars: 1 µm

4.2 HMM step height analysis

In this study, we analysed photobleaching time series using Hidden Markov Modelling (HMM). Previously, Messina and co-workers used HMM to analyse multichromophore

photobleaching time series (67). We, thus, sought to apply HMM analysis for *in vivo* near-TIRF time series.

An HMM is a stochastic model that maps measured values to unobserved (or hidden) states. A basic premise of HMMs is the Markov assumption, which states that state transitions occur stochastically and are completely determined by the transition probabilities. Photobleaching HMM analysis models each times series as an ordered state-sequence (cell intensity levels varying in time); we associate each state transition with photobleaching. We describe an HMM using the following parameters:

(1) π, an initial probability distribution, which describes the probability the system begins in each state.

(2) A, a transition probability matrix, which describes the probability a_{ij} of transitions from state i to state j.

(3) B, an observation probability distribution, which describes how likely an observation arises from each state.

Baum and colleagues developed an efficient algorithm to systematically obtain Markov chain parameter estimates; this is commonly referred to as Baum-Welch algorithm (68, 69). In our analysis, we are particularly interested in the state-sequence reconstruction, which allows us to identify intensity change points. We therefore used the Viterbi algorithm to determine the most likely state sequence (70, 71).

To begin our analysis, I manually selected time series such that single steps could be observed by eye (50% of the time traces). Here, time traces showing a slight continuous decrease at the last intensity level (stage drift) and very loaded cells ($\gg$ 10 labelled molecules) were neglected.

Due to the nature of the data (about 10 photobleaching steps), performing straightforward HMM analysis was not possible, $\mathcal{O}(TN^2)$, as computation-time is quadratic

with number of states N and linear with length of time series T. We thus developed a modified algorithm to recursively model an HMM, with each iteration removing all data belonging to the last photobleaching step. Each iteration allowed up to 10 states to be fit. Such a method took advantages of exponential photobleaching kinetics: the last photobleaching step was likely to last significantly longer than previous steps, and thus fitting the last step was likely to have the greatest data support. By only keeping the state values for the last step and then re-analysing the remaining data, we could iteratively improve our estimates for shorter steps. I manually confined algorithm accuracy and retained 71 out of 80 time series for further analysis. I provide a more detailed discussion of the HMM algorithm in sec. A.4.2.

I estimated the unitary intensity for a single ATTO647N dye from the step height distribution (i.e., absolute changes[1] in intensities at each state transition) for the 71 time series. I present the step height distribution (total number: 324) in fig. 4.2.

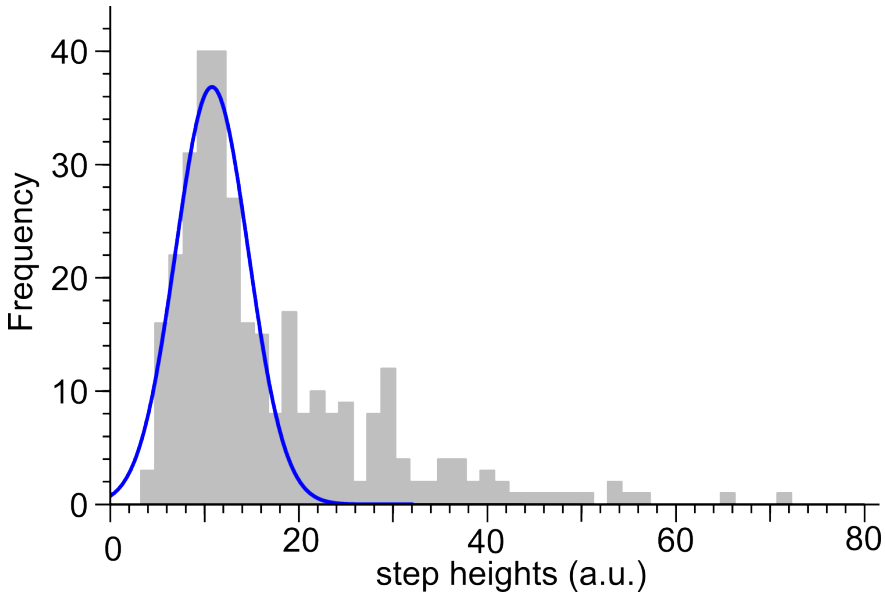

Figure 4.2: Step height distribution obtained from HMM analysis. A single gaussian fit (blue) of main data peak gives a single step height of 11$\pm$4 a.u.; my analysis consequently uses this step height as the single-molecule unitary intensity.

[1] I also observed fluorophore blinking etc.

The distribution shows a main peak at $\sim$ 10 a.u. and smaller peaks near 20 and 30 a.u. HMM analysis failed to often accurately resolve multiple photobleaching steps corresponding to the bleaching of 2 or more fluorophore molecules at the same time (or very closely). Such steps frequently occurred at the begin of the time series where exponential kinetics resulted in early steps lacking sufficient data support. As a result, noise had a greater impact on HMM analysis, resulting in greater variation in multi-photobleaching step heights. I fitted the step height distribution with all parameters without constraints. I interpreted the fitted mean as the single-molecule unitary intensity (11 ± 4 a.u. corresponding to 800 ± 300 photon counts per 100 ms).

4.3 Internalisation histograms

The single-molecule unitary intensity estimated to 11 a.u. was then used to calibrate initial cell intensities recorded under the same illumination conditions into actual numbers of internalised dsDNA ATTO647N molecules per cell. Cells were electroporated with 10 pmol and 100 pmol dsDNA ATTO647N and imaged in wide-field mode (continuous illumination, $P(\lambda = 638\,\mathrm{nm}) = 3$ mW, exposure time 100 ms). The normalised and baseline-subtracted initial (first frame after exposure) cell intensities were divided by the unitary intensity giving the number of internalised molecules. The number of internalised molecules per cell for 300 cells per sample were plotted in a histogram, fig. 4.3. Adding 10 pmol of DNA before electroporation, more than 80% of the cells were loaded[2] with fluorescent molecules whereas the cells of the non-electroporated negative control were in good agreement with empty cells. The first bin in the internalisation histogram accounts for cellular autofluorescence and can be seen as an offset. The histogram of internalised molecules per cell for the 10 pmol sample showed

[2]Cells are 'loaded', when they exhibit more fluorescence than two standard deviations above the autofluorescence of empty cells.

a wide distribution (mean: 121, std: 106, median: 87, range: 10-500 molecules). Increasing the amount of DNA to 100 pmol, the number of loaded molecules per cell increased as well as the wide distribution of internalised dsDNA (mean: 175, std: 187, median: 91, range: 10-700 molecules). I noticed that the empty cells (no dsDNA added and no electroporation) and the negative controls (no electroporation) showed little fluorescence signal corresponding to the cellular autofluorescence. Comparing the 10 pmol and 100 pmol histogram, I observed that significantly more cells of the 10 pmol sample were loaded with 50-150 DNA molecules and more cells of the 100 pmol sample were loaded with 400 and more molecules. Only about 70% of the cells were loaded in the 100 pmol sample. The negative control of the 100 pmol sample still compares very well with empty cells. The higher amount of non-loaded cells for the 100 pmol sample compared to the 10 pmol sample is likely to be caused by less efficient electroporation (data was acquired on a single day).

Varying the amount of fluorophores before electroporation and selecting cells dependent on their cell intensity gives a good control over the copy numbers of internalised molecules and thus the concentration of internalised biomolecules inside the cell can be estimated (rule of thumb: 1 molecule in *E.coli* $\sim$ 1 nM). This becomes important when studying reaction kinetics or even when establishing single-molecule tracking in live bacteria.

Contributions

I performed all the work in section 4.1 and 4.3. I carried out and analysed all photobleaching measurements (analysis software was written in MATLAB) in section 4.2. Kristofer Gryte performed the HMM analysis and I calculated the transition step heights and obtained the single-molecule unitary intensity.

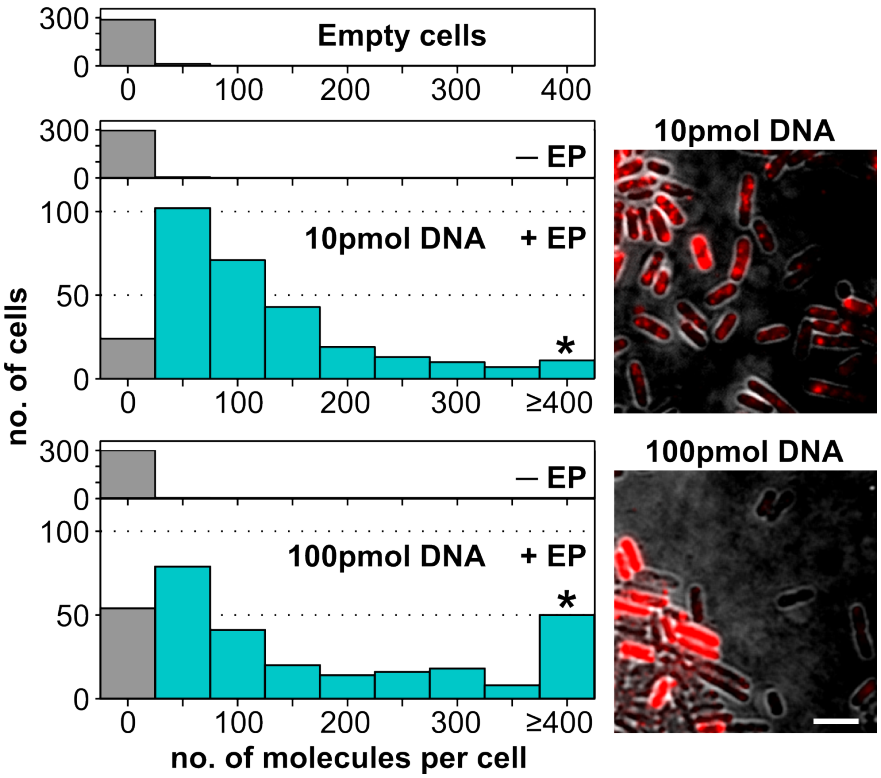

Figure 4.3: Histogram of internalised molecules per cell electroporated with different amounts of dsDNA ATTO647N. Molecule numbers were calculated from the initial fluorescence intensity divided by the single-molecule unitary intensity for 300 cells per sample. From top to bottom: electroporated empty cells, non-electroporated and electroporated cells incubated with 10 pmol and 100 pmol dsDNA. Empty and non-electroporated cells correspond to autofluorescence only. Electroporated cells show a broad distribution of internalised molecules, with a higher proportion of highly loaded cells at 100 pmol. The mean number for 10 pmol is 121±106 molecules. Right: Overlay of white-light and fluorescence channel for two example field of views. Scale bar: 3 µm

Chapter 5

In vivo single-molecule fluorescence studies

The quantification of internalised molecules allowed me to find settings to work at the single-molecule level in bacteria. Due to the use of the high brightness and photostability of organic fluorescent DNA fragments single-molecule tracking was performed. Single-molecule tracking for about 10 s and long-lived single-molecule fluorescence observation for about 10 min open new avenues to study diffusion paths or binding and unbinding events in live bacteria.

5.1 Tracking of dsDNA standards

First, I wanted to follow the movement of internalised biomolecules inside the bacterial cytoplasm at the single-molecule level. Using organic fluorophore labelled dsDNA standards, I was interested in the time regime where single-molecule diffusion studies can be carried out in live cells.

5.1.1 Long-lived single-molecule tracks

I electroporated *E.coli* cells in presence of 5 pmol dsDNA Cy3B and dsDNA Alexa647 and 2 pmol dsDNA ATTO647N. To track single-molecules for a long time, the cells were exposed to high laser powers (dsDNA Cy3B: $P(\lambda = 532\,\text{nm}) = 15\,\text{mW}$, dsDNA Alexa647: $P(\lambda = 638\,\text{nm}) = 15\,\text{mW}$, dsDNA ATTO647N: $P(\lambda = 638\,\text{nm}) = 23\,\text{mW}$) with a temporal resolution of 15 ms. The experiment was performed in widefield mode under continuous illumination to be able to capture the movement of the single-molecule within the bacterial cytoplasm.

To work at the single-molecule level, a smaller amount of labelled DNA molecules were electroporated compared to the cell-based internalisation efficiency studies. Moreover, the cell samples were pre-bleached with the excitation laser light before acquisition was started until the density of fluorescent molecules allowed single-molecule tracking (rule of thumb: 2-5 molecules per cell depending on the cell size). All the tracking analysis was performed using a custom-written Matlab script described in sec. A.4.3 and (72). Briefly, the point spread functions (PSFs) of all single molecules were localised in each frame. To get the molecules' positions, the PSFs were fitted with an elliptical 2D Gaussian. Since such localisation algorithms perform best for fluorophore densities less than $1\,\text{fluorophore}/\mu\text{m}^2/\text{frame}$ (8), only cells loaded with about 3 (ideally less than 3) fluorescent dyes were analysed. For tracking of individual molecules, the fitted PSFs were linked when they appeared in two consecutive frames within a tracking window of 7 pixels ($\sim 0.67\,\mu\text{m}$). A memory parameter of 1 frame was used to account for missing the PSF in one frame.

In fig. 5.1, examples of single-molecule tracks lasting for more than 6 s in the case of dsDNA Cy3B, 5.1 A and dsDNA ATTO647N 5.1 B are shown. Furthermore, I show a $\sim 3\,\text{s}$ single-molecule track for dsDNA Alexa647 5.1 C. The number of photons per exposure time (integral of Gaussian fitted PSF over background divided by

the gain factor of $4.55\,\mathrm{counts/photon}$) was plotted for each movie frame where the single-molecule was tracked. Each single-molecule track was visualised within the cell outline. I note that the same time dependent colour code for all three tracks was used to highlight the diffusion paths of the single molecules in the cellular cytoplasm over time.

Although the initial amount of labelled DNA prior to electroporation was decreased and the cells were pre-bleached before acquisition, $<$ 20% of the cells showed a sufficient low density of fluorescent molecules for particle tracking (ideally only one fluorescent molecule per cell) at the time of acquisition. This can be explained by the wide distribution of internalised DNA molecules per cell; already discussed in sec. 4.3. Furthermore, single-molecule localisations between three consecutive frames were sometimes missing, cutting the tracks into shorter parts. When increasing the memory parameter to 3 frames within the tracking algorithm, the presented single-molecule tracks could be extended to $8.8\,\mathrm{s}$ for dsDNA Cy3B and to $8.4\,\mathrm{s}$ for dsDNA ATTO647N. Since the Alexa647 dye is more subject to blinking (29, 30) single-molecule tracking could not be extended.

It is important to point out that through the pre-bleaching of the samples, I was already bleaching large amounts of loaded single molecules. This enabled us to work at the single-molecule level but also drastically reduced the actual time of single-molecule tracking down to about $10\,\mathrm{s}$ and thus decreasing the chance to observe even longer lasting single-molecule tracks *in vivo*. Thus, we believe that single-molecule tracking can be extended to up to several tens of seconds. This can be achieved by better controlling the copy number of fluorescent biomolecules inside the cell down to one activated molecule at a time and tracking the molecule until its photobleached.

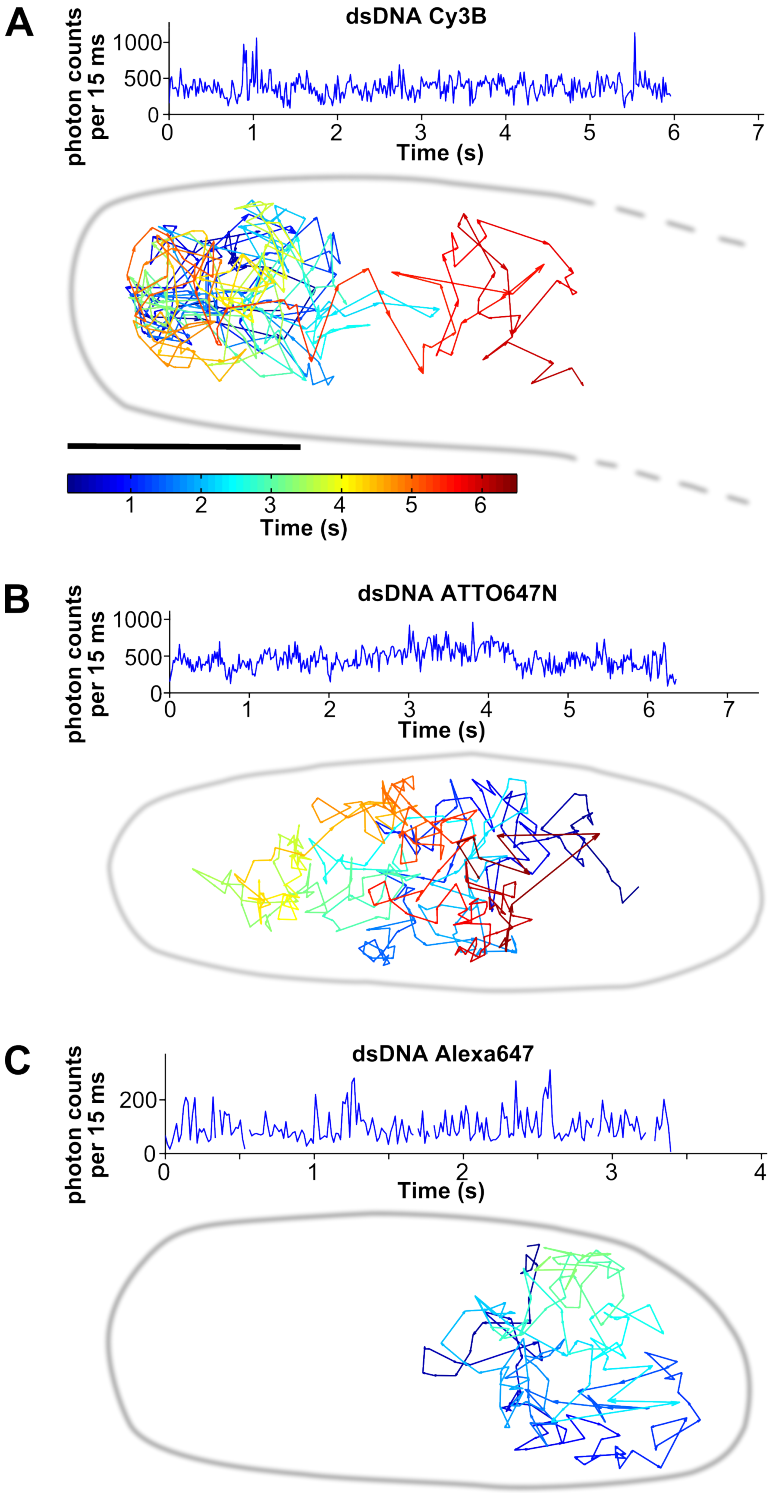

Figure 5.1: Single-molecule time traces and trajectories of diffusing dsDNA labelled with three different fluorophores (**A**. Cy3B, **B**. ATTO647N and **C**. Alexa647). Time traces of photon counts per 15 ms exposure (blue) show fluctuations mainly caused by molecular diffusion. Time-coloured trajectories show single molecules tracked for several seconds exploring the cell volume (grey boundary) were plotted within the cell boundary. Scale bar: 1 µm

5.1.2 Diffusion studies

Second, I was interested in the quantification of the movement of single molecules inside the cell. At this stage, distinguishing localised from diffusing single-molecule species and getting an idea how the dsDNA diffusion is dependent on the dye property were the main aims.

For diffusion analysis, I loaded *E.coli* cells with $10\,\mathrm{pmol}$ of dsDNA Cy3B, $10\,\mathrm{pmol}$ of dsDNA ATTO647N and $2.5\,\mathrm{pmol}$ of dsDNA Alexa647. The cells were imaged on the agarose pad under continuous illumination (Cy3B: $P(\lambda = 532\,\mathrm{nm}) = 2\,\mathrm{mW}$, ATTO647N and Alexa647: $P(\lambda = 638\,\mathrm{nm}) = 1\,\mathrm{mW}$) with an exposure time of $10\,\mathrm{ms}$ in near-TIRF mode. This illumination mode was used to gain a better signal-to-noise ratio. The uneven illumination of the cells resulting in the shortening of tracks when molecules move out of the cell's illuminated part were not a problem since only tracks longer than 3 steps were used for diffusion analysis such that no noise was picked up. For tracking analysis, the memory parameter was set to 'zero'-frames as well to avoid miss-linking of molecules moving in and out of the illumination plane.

From single-molecule tracking the mean-squared displacement (MSD) of a single track, the average of the MSDs of each step $\overline{\mathrm{MSD}}$, was calculated. From the $\overline{\mathrm{MSD}}$ an apparent diffusion coefficient was calculated, assuming 2D Brownian motion $D_{\mathrm{app}} = \frac{\overline{\mathrm{MSD}}}{4\Delta t}$ with frame time Δt. The apparent diffusion coefficient of many tracks were plotted in an apparent diffusion coefficient histogram where localised molecules were represented by an apparent diffusion coefficient of about zero. The principle of the diffusion analysis is described in more detail in sec. A.4.3 .

For each sample, dsDNA labelled with Cy3B, ATTO647N and Alexa647 in 11, 13 and 30 fields of view were analysed, respectively. The cells showing a low density of internalised molecules for single-particle tracking were manually selected, i.e. cells (about 5 cells per FOV) were individually cropped and the first frame for tracking

analysis was chosen. The tracks for all analysed cells were collected and for each track an apparent diffusion coefficient was calculated from the $\overline{\text{MSD}}$.

Fig. 5.2 shows the apparent diffusion coefficient histograms for all three samples. For the dsDNA Cy3B, dsDNA ATTO647N and dsDNA Alexa647 sample a total number of 2117 tracks (from $\sim$ 30 cells), 4257 tracks (from $\sim$ 40 cells) and 1214 tracks (from $\sim$ 60 cells) were observed respectively.

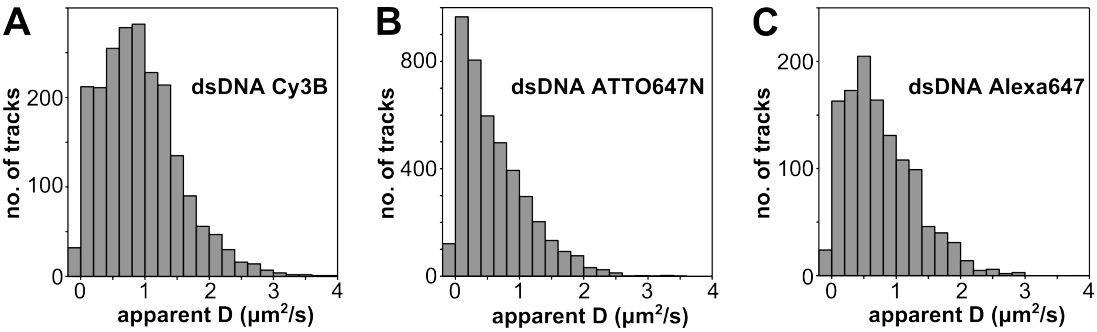

Figure 5.2: Apparent diffusion coefficient histogram for green (**A**. Cy3B) and red (**B**. ATTO647N and **C**. Alexa647) labelled dsDNA molecules. The apparent diffusion coefficient was calculated from the mean squared displacement of each track ($D_{\text{app}} = \frac{\overline{\text{MSD}}}{4\Delta t}$, Δt: frame time). For dsDNA Cy3B, dsDNA ATTO647N and dsDNA Alexa647 a total number of 2117 tracks (from $\sim$ 30 cells), 4257 tracks (from $\sim$ 40 cells) and 1214 tracks (from $\sim$ 60 cells) were analysed respectively. Cy3B labelled dsDNA exhibits faster diffusion than ATTO647N and Alexa647.

The apparent diffusion coefficient histogram for dsDNA Cy3B, fig. 5.2 A, showed a major peak at about $D_{\text{app}} = 0.9\,\mu\text{m}^2/\text{s}$. From diffusion studies of *E.coli* DNA Polymerase I (DNA PolI, 103 kDa, (73, 74)) using photoactivatable PAmCherry as a label analysed with the same software, a similar apparent diffusion coefficient of about $D_{\text{app}} = 1\,\mu\text{m}^2/\text{s}$ for Pol I was measured which matches a simulated 2D Brownian motion with diffusion coefficient of $D_{\text{PolI}} = 1.75\,\mu\text{m}^2/\text{s}$ (data not shown, Uphoff et al. (72)). This would imply that we may be looking at diffusion of dsDNA bound to larger proteins comparable in size to Pol I which is likely since I was using non-protected/stabilised dsDNA fragments. The DNA end can provide a binding site for nucleases and repair enzymes evolved to recognise foreign or damaged DNA.

The dsDNA ATTO647N sample showed a larger population of localised molecules with a low apparent diffusion coefficient, $D_{\text{app}} < 0.4\,\mu\text{m}^2/\text{s}$, such that it is hard to distinguish between the diffusing and localised species, fig. 5.2 B. The dye ATTO647N is known for its hydrophobicity and is therefore more likely to stick to membrane structures (39). This has to be kept in mind when using ATTO647N as a label. Nevertheless, the single-molecule track in fig. 5.1 shows that diffusing dsDNA ATTO647N molecules could be observed. Furthermore, comparing the apparent diffusion coefficient histogram, fig. 5.2 A and B, shows that the tracking analysis can be used to distinguish between diffusing and localised molecule species.

The apparent diffusion coefficient histogram of dsDNA labelled with Alexa647, fig. 5.2 C, shows a peak at about $0.5\,\mu\text{m}^2/\text{s}$. Here like in the case of dsDNA Cy3B, the diffusion of the dsDNA fragment bound to DNA binding proteins might have been observed. Since Alexa647 had a really short photobleaching lifetime ($\sim 1\,\text{s}$ on average) under these illumination conditions and especially when pre-bleaching the cells, I struggled to get good statistics for the apparent diffusion coefficient histogram. Although I analysed twice as many cells compared to the dsDNA Cy3B sample I only obtained half as many tracks. During acquisition and manual cell selection fluorophore blinking was observed which overestimated the number of tracks corresponding to localised molecules, since each localised track was counted again for each blinking event. For the diffusing molecule species blinking cannot be distinguished from diffusing out of the illuminated cell volume. Nevertheless, the Alexa647 dye shows better diffusion properties than the ATTO647N dye, but is not as photostable.

It is also important to point out that we are probably unable to detect and track totally freely diffusing 45-bp dsDNA fragments in such a confined cellular volume. Measurements with the 45-bp dsDNA fragment labelled with ATTO647N were carried out *in vitro* in a buffer containing 50% glycerol under near-TIRF illumination and with an

exposure time of 10 ms. A similar diffusion coefficient analysis revealed a wide apparent diffusion coefficient distribution centred on $7\,\mu m^2/s$ (data not shown). I never observed such high apparent diffusion coefficient of the internalised dsDNA standards in *E.coli*.

From this study, Cy3B shows good performance for a molecule label for diffusion studies *in vivo* in the green spectral range. For the red spectral range the dye Alexa647 is superior to the dye ATTO647N for pursuing diffusion studies. We note that for the diffusion studies the purity of the labelled dsDNA sample (no free dye) and the washing step after recovery are crucial, since free dye or labelled dsDNA sticking to the outer membrane cannot be distinguished from localised dsDNA molecules inside the cellular cytoplasm. Here, the DNA purification and electroporation protocol can still be optimised.

To conclude, diffusion paths of single molecules were observed for up to 6 s and evidence was given that single-molecule tracking can be extended up to several tens of seconds. This opens new biological relevant observation time regimes that are at least an order of magnitude larger compared to fluorescent proteins (several hundredths of a second (38)). For instance, we can observe processes on the timescale of gene expression ($\sim 2\,s$) etc. and the influence of transcription factors on gene expression can be studied in real-time. Furthermore, the apparent diffusion coefficient analysis allows the distinction between localised and diffusing molecules and gives a tool to distinguish binding from unbinding events.

5.2 Observation of long-lived single-molecule fluorescence

Here, I am addressing the extension of single-molecule fluorescence observation under continuous illumination in live bacteria using organic fluorophores. Therefore, mainly the excitation laser power was reduced to prevent early bleaching and the exposure time was increased allowing still single-molecule detection in the minute time regime. This approach is sufficient for observing the transient binding of molecules of interest to cellular structures or slow diffusing molecule species.

E.coli were electroporated with 2.5 pmol of dsDNA ATTO647N and imaged with laser powers of $P(\lambda = 638\,\text{nm}) = 300\,\mu\text{W}$, 600 µW and exposure times of 100 ms and 50 ms respectively in near-TIRF mode. The near-TIRF mode was chosen because of the better signal-to-noise ratio. In addition, the back-reflection of the excitation laser light on the glass cover slide was needed to stabilise the z-position of the microscope stage and avoiding loss of the focus during observation. The back-reflection signal was detected providing a feedback signal for the closed-loop positioning system that actively controls the focus of the microscope (continuous reflective-interface feedback focus system, CRIFF, Applied Scientific Instrumentation, Eugene, Oregon, USA). The microscope stage stabilisation using the CRIFF system was used for these sensitive single-molecule observations lasting up to 25 min.

While maintaining exposure times of 50-100 ms, I was able to observe individual localised dsDNA ATTO647N for about 10 min under continuous illumination, fig 5.3 A and B. In fig. 5.3 C an individual molecule was observed for more than 25 min under continuous illumination with an exposure time of 100 ms. The single molecules were localised and tracked and the time traces show the photon count per exposure time of the single molecule until photobleaching. The photon count is the integral of the fitted

2D elliptical Gaussian to the PSF divided by the gain factor of 4.55 counts/photon.

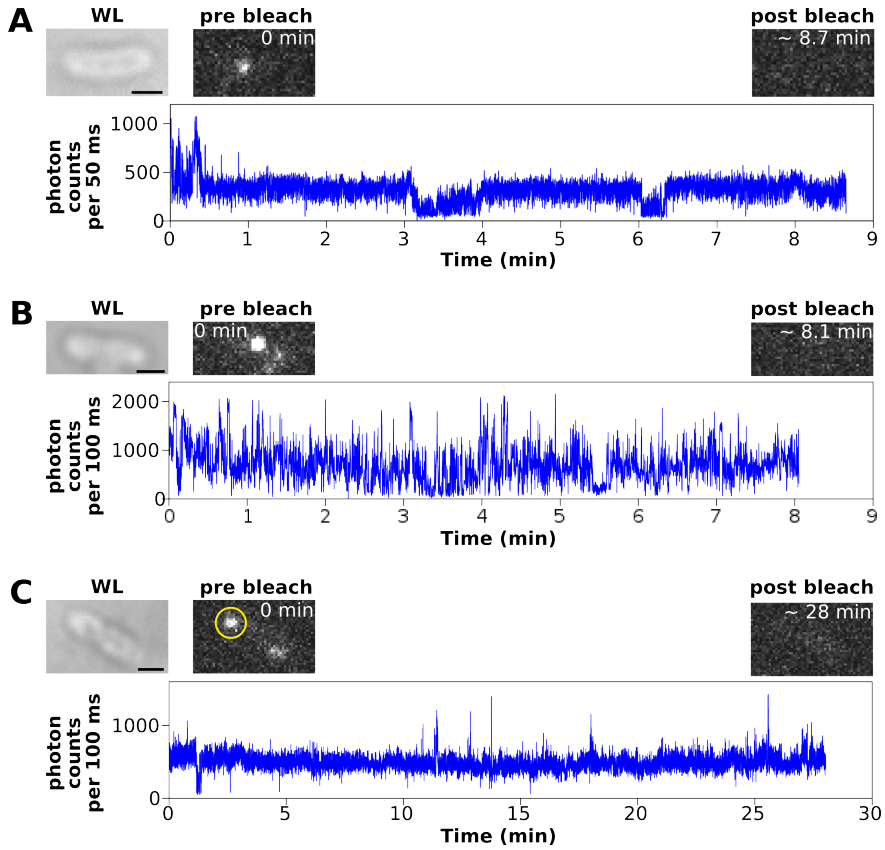

Figure 5.3: Long-lived single-molecule observation of dsDNA ATTO647N. Time traces of single-molecule photon counts per exposure time (blue) and cell images insets for 3 different molecules measured in live *E.coli* are shown. **A**. Single-molecule observation for more than 8 min with 50 ms time resolution. **B**. Single-molecule observation for 8 min exhibiting blinking behaviour. **C**. Single-molecule observation for about 28 min with 100 ms time resolution. Insets: White-light (WL) image of the cell and fluorescence image at the start of acquisition and after photobleaching. The yellow circle highlights the molecule of interest, if not distinct. Scale bars: 1 µm

Different features were observed in the photon count time traces that can be related to single-molecule behavior observed in the raw data movie. The drop in photon counts per exposure time especially in time trace fig. 5.3 A was related to movement of the single molecule mainly further out of the excitation field (z-movement). Changes in photon counts per exposure time on fast time scales, like in time trace fig. 5.3 B between 2 to 4 min, were caused by fluorophore blinking. I note, that the long-lived single-molecule time traces fig. 5.3 C lasting for more than 25 min was only observed

once, whereas 8 min time traces were observed on an average basis.

To get an idea of the probability to observe a single molecule under these illumination conditions for 10 min or even 25 min cell-based photobleaching studies were carried out under these illumination conditions. There, 10 pmol dsDNA ATTO647N were loaded into *E.coli* and the cells were imaged in near-TIRF illumination under continuous illumination ($P(\lambda = 638\,\text{nm}) = 300\,\mu\text{W}$, 100 ms).

The analysis was carried out similarly to the cell-based photobleaching experiment in sec. 4.1. The cell intensity per cell area over time was calculated for 312 cells. Fig. 5.4 shows the average photobleaching time trace with standard deviation error bars (blue) and two representative individual cell-based photobleaching time traces (grey).

In the average time trace and the individual time traces two regimes in fluorescence decay were observed. Until about 0.5 min the fluorescence decays rapidly whereas afterwards a second larger photobleaching lifetime was observed. Up to now, we do not really understand the two regimes. The bleaching of the cellular autofluorescence could be excluded, since it was measured for 350 empty cells under the same illumination conditions resulting in a photobleaching lifetime in the order of 1 s. One explanation could be the uneven illumination of the cell through the near-TIRF illumination (exponential decaying excitation field). This would bleach fluorophores in the part of the cell closer to the cover slide rapidly whereas the rest of the fluorophores would be exposed to less intense laser light and thus show a longer photobleaching life time. Understanding this phenomenon could lead to an assay to characterise the near-TIRF illumination. This could be used as a calibration for the near-TIRF illumination which we need for the reproducibility of our measurements and is still missing in the single-molecule field. Furthermore, photophysical properties of the ATTO647N dye *in vivo* have to be understood.

To simplify the photobleaching analysis and limit the number of fitting parameters, for instance to prevent fitting two single exponential decays with different lifetimes, we decided to fit a single-exponential decay to each individual photobleaching time trace giving an estimate for the *in vivo* photobleaching lifetime. The fits for the average photobleaching time trace and the two example time traces were plotted in fig.5.4 in red. The 312 photobleaching lifetimes were plotted in a histogram, inset fig. 5.4, resulting in a mean *in vivo* photobleaching lifetime of $\tau_{in\ vivo} = 1.5 \pm 0.6\,\mathrm{min}$.

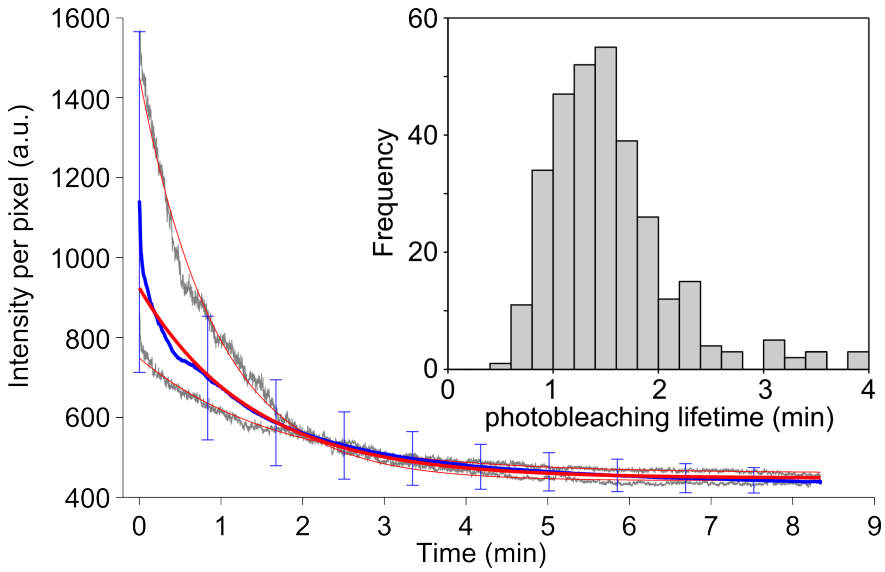

Figure 5.4: Cell-based photobleaching studies of 10 pmol dsDNA ATTO647N (312 cells in total). Main graph: Averaged photobleaching time trace with standard deviation error bars (blue) and two individual cell-based photobleaching time traces (grey). Single exponential fits (red) were performed starting from data point 500. Inset: Distribution of photobleaching lifetimes gained from individual photobleaching time trace fits.

To relate the observed *in vivo* photobleaching lifetime of ATTO647N, I performed *in vitro* measurements with the same dsDNA ATTO647N (B17) fragment. Therefore, the dsDNA molecule were immobilised on the glass cover slide as described in sec. A.2.3. The dsDNA fragment with labelling position B17, 28 bp from biotin linker, was used to avoid dye interference with the glass cover slide. Five FOVs were recorded under the same illumination conditions and each photobleaching time trace

(ensemble intensity of whole FOV over time) was fitted with a single exponential. A mean *in vitro* photobleaching lifetime of $\tau_{\textit{in vitro}} = (3.1 \pm 0.8)\text{min}$ was obtained. The observed *in vitro* photobleaching lifetime is higher compared to the photobleaching lifetime observed *in vivo*. The lower photobleaching lifetime *in vivo* can be explained by the different sample preparation and the different impact of the uneven near-TIRF illumination. Furthermore, the impact of the reducing cellular environment on the dye properties is not yet fully understood and further studies have to be carried out.

Observing an average *in vivo* photobleaching lifetime of $\sim 2\,\text{min}$ for ATTO647N under continuous illumination ($P(\lambda = 638\,\text{nm}) = 300\,\mu\text{W}$, near-TIRF mode), I used this value to calculate the chance of observing a single molecule after $10\,\text{min}$ under the same conditions; the probability is given by $\exp(-\frac{10\,\text{min}}{2\,\text{min}}) = 0.007$.

This means about 150 molecules have to be internalised to statistically observe one molecule lasting for $10\,\text{min}$ under these conditions. The internalisation of 150 molecules per cell is a good assumption for the electroporation of cells with $10\,\text{pmol}$ dsDNA ATTO647N (see internalisation histogram, fig. 4.3). From this calculation a time trace lasting for $25\,\text{min}$ has a very low probability of $4 \cdot 10^{-6}$. To put this value into context, the observation of 600 cells given $10\,\text{pmol}$ dsDNA ATTO647N internalisation ($\sim$ 150 molecules per cell) would give a probability of about $1.3 \cdot 10^{-6}$ to observe such a long-lived fluorescent molecule. These calculations are in good agreement to my experimental experiences.

In this section I extended fluorescence observation at the single-molecule level to about $10\,\text{min}$ in live bacteria maintaining temporal resolution of down to $50\,\text{ms}$. Being now able to study processes in the minute time regime opens new biological applications. It should be now possible to observe gene transcription taking about $2\,\text{min}$ per gene in real-time. Furthermore, processes within the cell division cycle (division time of $30\,\text{min}$, sec. 3.2) can be studied.

Contribution

I performed all the experiments and analysed the data. The gain measurement on the optical setup was carried out by Justin Pinkney and the value was kindly provided to the lab. The localisation and tracking software is based on a version by Stephan Uphoff (72). I adapted the Matlab scripts for my type of data and implemented further features such as to load tif-files as input, implemented a threshold and filter parameter check before localisation and wrote a script to visualise the tracked molecules in a movie tif-stack on top of the raw data to get an idea of which molecules were picked up.

Chapter 6

Conclusion and Outlook

In this work, electroporation was introduced as an efficient and high throughput internalisation method of biomolecules such as 45-bp dsDNA fragments labelled with organic fluorophores into live bacteria. The efficient internalisation of different amounts of dsDNA labelled with different organic fluorophores covering the green (Cy3B) and red spectrum (ATTO647N and Alexa647) was presented. The negative controls where the labelled dsDNA were added but not electroporated showed only fluorescence signal comparable to the autofluorescence of empty cells proving that the fluorescently labelled DNA molecules do not stick to the outside of the cell membrane. The cells showed a very good viability after electroporation; we observed about 50% dividing and less than 5% compromised cells. This gives good evidence that we are actually able to study the introduced biomolecules in *in vivo* settings. Furthermore, we observed the increase in fluorescence due to the expression of the fluorescent protein EmGFP upon internalisation of T7 RNA polymerase. This assay proved that the electroporated biomolecules are functional, inside the cellular cytoplasm and that even proteins of about 100 kDa can be internalised.

To get a better control for my *in vivo* studies, I estimated the number of internalised biomolecules by carrying out single cell-based photobleaching measurements. By

means of HMM analysis, we obtained the single-molecule unitary intensity through which initial cell intensities can be related to actual numbers of internalised molecules. So, I observed a wide distribution of internalised biomolecules per cell ranging from one to several hundreds of biomolecules depending on the amount of added fluorescent molecules prior to electroporation. A high internalisation efficiency of more than 70% was obtained for the dsDNA standard. The HMM analysis method is still not robust and input time series have to be manually pre-selected. At this early stage of the analysis development not all the information of the system (e.g. state transitions mainly due to photobleaching) were introduced in the model. Thus, the performance of the HMM analysis can still be optimised and speeded up.

As a first characterisation of the fluorescence signal obtained from an internalised single molecule, I tracked individual dsDNA standards with a time resolution of $15\,\mathrm{ms}$ within the cellular environment. For dsDNA Cy3B and dsDNA ATTO647N diffusing single molecules were observed for up to $8\,\mathrm{s}$. The lower photostability mainly due to blinking of Alexa647 only allowed the observation of tracks for about $3\,\mathrm{s}$ for the dsDNA Alexa647 sample. The diffusion study of the dsDNA standards revealed lower apparent diffusion coefficients as expected, letting us to believe that we observed diffusion of dsDNA fragments (labelled with Cy3B and Alexa647) bound to larger DNA binding proteins and thus slowing down the diffusion. The dsDNA ATTO647N sample exhibited more localised tracks due to known hydrophobicity of the dye. Thus, the dyes Cy3B and Alexa647 have to be preferred for *in vivo* diffusion studies.

We believe that the performance of the diffusion analysis could be improved by introducing photoswitching of the fluorophores *in vivo* and so controlling the number of activated dyes per cell to one molecule at a time (8, 29). This will be even easier to achieve since the diffusion analysis can be carried out with short tracks (> 3 steps) already. Thus, the cross-linking of tracks of localised and diffusing molecules

will be reduced and we could come up with an apparent diffusion coefficient threshold to distinguish both species. Furthermore, introducing '*in vivo* DNA standards', i.e. protected DNA fragments such as those containing hairpin loops or unnatural chemical groups (e.g. phosphorothioates) and containing little sequence similarity to the *E.coli* chromosome to minimise binding by endogenous proteins, is necessary for further diffusion studies to distinguish between free DNA diffusion and diffusion of DNA-protein complexes. The '*in vivo* DNA standards' can then be used to probe for instance different dye properties, dye positions and DNA lengths *in vivo* and their influence on the apparent diffusion coefficient distribution.

Maintaining a temporal resolution of down to $50\,\mathrm{ms}$, localised single dsDNA ATTO647N molecules were observed for about $10\,\mathrm{min}$ in the cell pushing single-molecule observation to the minute time scale and thus opening new avenues to study biological systems *in vivo* at the molecular level.

The electroporation of organic fluorescent labelled biomolecules into live cells provides a powerful tool to transfer and investigate a well characterised biological system already studied *in vitro* into a cellular environment. The high photostability and brightness of organic fluorophores ($>$10x brighter than fluorescent proteins (75)) can be applied to single-molecule tracking studies. *In vitro* labelling protocols can be kept and the single-molecule observation can be moved to a natural context.

This method allows us to study biological mechanisms inside the bacterial cell using organic fluorophores; a tool the single-molecule fluorescence field is missing up to now and which will hopefully be adopted by the community.

Future work

Generally, electroporation conditions can still be optimised (e.g. modification of the applied electric field) to achieve even higher internalisation efficiencies. The lag-time between the electroporation and the start of the measurement due to the re-

covery step could be minimised for *in vivo* studies and the amount of internalised biomolecules could be better controlled. Furthermore, we have to get a better control on the number of acitvated fluorophores per cell; preferably one activated molecule per cell per frame. This could be achieved by the introduction of photoswitching the organic fluorophores *in vivo*. This would improve the tracking analysis, allow a better understanding of apparent diffusion coefficient distributions and help to distinguish for instance binding and unbinding events within a single-molecule track. Moreover, introducing photoswitching of the internalised fluorophores would allow the implementation of localisation-based super-resolution imaging and thus spatial resolution of down to 20 nm (13) could be obtained. With the internalisation of doubly labelled biomolecules, the observation of conformational changes in the 2-10 nm range become possible using FRET assays. Here, the cellular autofluorescence and the potential fast diffusion behaviour of the biomolecule inside the cell are the major challenges.

Appendix A

Materials and methods

A.1 DNA standards: sequences and handling

A.1.1 DNA sequences

Oligonucleotides used were prepared by automated synthesis from IBA GmbH, Göttingen, Germany.

Sequences shown from 5' to 3':

TOP strand (unlabelled): TAA ATC TAA AGT AAC ATA AGG TAA CAT AAC GTA AGC TCA TTC GCG – biotin

TOP strand – Cy3B: Cy3B TAA ATC TAA AGT AAC ATA AGG TAA CAT AAC GTA AGC TX/CA TTC GCG – biotin

BOTTOM strand (unlabelled): CGC GAA TGA GCT TAC GTT ATG TTA CCT TAT GTT ACT TTA GAT TTA

BOTTOM strand – B 17 – ATTO647N: CGC GAA TGA GCT TAC G **ATTO647N** TTA TGT TAC CTA TGT TAC TTT AGA TTT A

BOTTOM strand – B 28 – ATTO647N: CGC GAA TGA GCT TAC GTT ATG TTA CCT **ATTO647N** ATG TTA CTT TAG ATT TA

BOTTOM strand – B 38 – ATTO647N/Alexa647: CGC GAA TGA GCT TAC GTT ATG TTA CCT TAT GTT ACT T **ATTO647N/Alexa647** AGA TTT A

A.1.2 DNA labelling

Labelling at the 5'-end of the TOP strand was performed using the 5'-amino-C6-modifying group with n-hydroxy-succinimidyl esters of Cy3B (GE Healthcare, Uppsala, Sweden). Internal labelling with ATTO647N (ATTO-TEC GmbH, Siegen, Germany) was performed using the same protocol for the three different BOTTOM strands B 17, B 28 and B 38. The internal labelled BOTTOM strand B 38 Alexa647 was purchased from IBA (IBA GmbH, BioTAGnology, Göttingen, Germany).

For labelling, 5 nmol of ssDNA (50 µL out of 100 µM stock) was precipitated by adding 5 µL of 5 M sodium chloride (NaCl) and 125 µL of ice-cold 100% ethanol and storing the mixture at -80 °C for longer than 30 min and spin down at 16 000 g, 4 °C for 15 min. The supernatant was removed and was gently rinsed with 200 µL ice-cold 100% ethanol before another centrifuge run of 10 min. The supernatant was removed and the pellet was let dry on the heating block at 37 °C to evaporate excess. Then, the pellet was dissolved in 100 µL sodium borate ($NaBO_3$, 0.1 M, pH 9.0).

For end labelling (Cy3B–TOP strand), ten-fold excess of dye (50 nmol of dye dissolved in 5 µL DMSO) were added to the DNA; wrapped in foil and placed on a shaker for 5 h or overnight. Internal labelling (ATTO647N–BOTTOM strands) was performed by incubating ten-fold excess of dye at 50 °C for 2 h or longer. Then another ten-fold excess of dye was added and incubated again as before.

The ssDNA was precipitated in 250 µL ice-cold 100% ethanol and 10 µL of 5 M NaCl at -80 °C for a minimum of 30 min; again centrifuged at 16 000 g, 4 °C for 15 min,

rinsed with 200 µL ice-cold ethanol and let dry at 37 °C. The pellet containing labelled and unlabelled DNA was then PAGE purified, see A.1.3.

A.1.3 DNA purification

The 45-bp ssDNA fragments were purified using a denaturing polyacrylamide gel electrophoresis (PAGE). An acrylamide concentration of 20% was used creating a 3D matrix of cross-linked hydrocarbons after polymerisation. The negatively charged labelled DNA was separated from the unlabelled DNA population and the free dye by applying an electrostatic potential across the neutral gel depending on the relative pore size. The gel was run at 550 V for 6 h in TBE buffer (89 mM Tris, 89 mM Boric Acid and 2 mM EDTA). The main labelled DNA fraction was cut out, crushed and eluted in double distilled water over night. The gel fragments were removed by centrifugation and filtering with a 0.45 µm pore size spin column. The DNA filtrate was then de-salted in a p6 column into water and was then evaporated in speedvac to near pellet.

A.1.4 DNA annealing

The dsDNA standards labelled with either Cy3B–TOP strand or ATTO647N/Alexa647–BOTTOM strand were prepared by annealing labelled TOP strand to unlabelled BOTTOM strand and unlabelled TOP strand to labelled BOTTOM strand, respectively. The oligonucleotides were annealed in a low-salt annealing buffer (20 mM Tris-HCl (pH 8.0), 10-100 mM NaCl, 1 mM EDTA) by heating to 94 °C and subsequent cooling to 4 °C over 45 min in steps of 10 °C.

A.2 Sample preparation

A.2.1 Electroporation protocol

Up to 5 µL of labelled dsDNA standards stored in the low-salt annealing buffer, 10 µM stock concentration, were added to 20 µL of electrocompetent cells (ElectroMAX™ DH5α-E™ Competent Cells, Invitrogen/ Life technologies, Carlsbad, California, USA) to a final amount of 1 to 100 pmol and incubated for 10 min on ice. The cell suspension and the organic fluorophore labelled biomolecules were added into the gap (width of 0.1 cm) of a pre-chilled electroporation cuvette. The cell suspension was then exposed to the discharge of a high voltage electric field. For all experiments carried out in this thesis, the initial electric field of 18 kV/cm decayed with a time constant of 5 ms. The cells were rapidly recovered in 500 µL of rich medium (super optimal broth with catabolite repression, SOC) for about 20 min shaking at 37 °C. Then, the cells were washed 5 times with phosphate buffered saline (PBS) by pelleting the cells by centrifugation at 3300 g for 1 min at 4 °C and then resuspension. Finally, the cells were resuspended in 100-200 µL PBS and stored on ice.

A.2.2 *In vivo* cover slides

The 1% agarose-M9 pads were prepared by adding 500 µL of the heated agarose-M9-salt medium on a glass cover slide and let cool. The cells were vortexed briefly to limit any potential of cell clustering. About 10 µL of the cell suspension were spread on the agarose pad. Finally, a burned cover slide was placed on top of the agarose pad which was turned towards the immersion oil objective for imaging.

For long-term observation of cells for several hours (viability check of the cells) the 1% agarose pad was prepared with M9 salts and EZ rich defined medium. Furthermore, a channel system was cut out off the pad, fig. A.1, and the agarose was kept wet by

adding about 100 µL EZ rich defined medium into the channel system every 90 min. Another attempt of cell immobilisation for imaging was to use polylysine or polyethyleneimine coated glass cover slides; incubation time of 5 min at room temperature in silicon gasket wells on glass cover slide and washed with PBS twice. But the cells were not always evenly attached to the coated cover slide and often were partially moving. Nevertheless, this method gives better access to the cells for buffer exchange around the cells compared to the agarose pad.

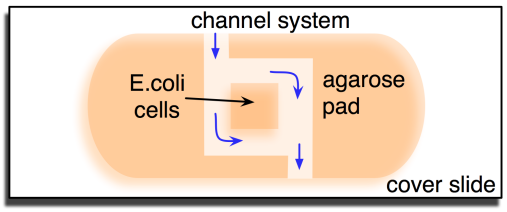

Figure A.1: Schematic of cutted channel system in agarose pad for buffer supply throughout the observation.

A.2.3 *In vitro* cover slides

For *in vitro* dsDNA ATTO647N photobleaching experiments in sec. 5.2 biotinylated dsDNA molecules were immobilised on neutravidin-biotinylated-BSA (bovine serum albumin) glass cover slides, fig. A.2.

Silicon wells were placed on burned cover slides and washed with 30 µL PBS twice. Then, 30 µL of biotinylated BSA (2 mg/mL) were incubated for 2 min in each well. After removal, the wells were washed twice with PBS again. Incubation of 30 µL neutravidin for 1 min was performed already on the microscope stage and was followed by the PBS washing step. The dsDNA ATTO647N (B17) was diluted down to 100 pmol in the annealing buffer containing BSA (20 mM Tris (pH 8.0), 1 mM EDTA, 500 mM

NaCl, 0.1 mg/mL BSA). After addition of 30 µL of 100 pmol dsDNA ATTO647N in the well, the surface coverage with dsDNA was followed through the microscope in the fluorescence channel. The dsDNA incubation was stopped when a good single-molecule density was achieved by washing the well twice with PBS.

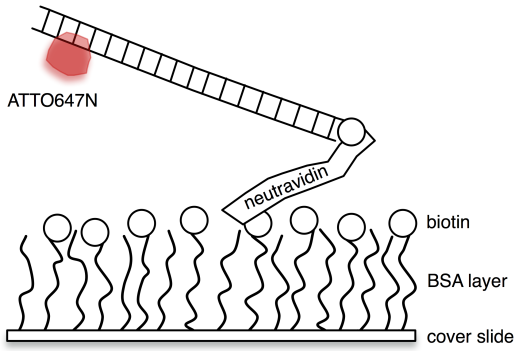

Figure A.2: Schematic of dsDNA labelled with ATTO647N immobilisation on glass cover slide

A.3 Optical setup and data acquisition

All measurements were carried out on two custom-built inverted total internal reflection fluorescence (TIRF) microscopes under continuous illumination. Since all experiments could have been carried out on any of these two microscope setups the imaging principle will be explained in more detail using only one setup. A schematic of the setup is shown in fig. A.3.

The general idea of any fluorescence microscope setup is to excite the fluorophore/sample with a specific bandwidth and collect the emitted fluorescent light filtered from the excitation light for instance on a camera chip. Thus, the setup can be divided into an excitation module, sample module and emission module.

The red diode laser (Vortran Stradus, 140 mW, Vortran Laser Technology, Sacramento, California, USA) emitted at 638 nm and could be directly modulated. The laser

intensity could be controlled by provided software. The green diode-pumped solid state laser (Cobolt Samba, 100 mW, Cobolt, Solna, Sweden) was also directly modulatable and emitted at 532 nm. The green excitation intensity was controlled by two neutral density filters. Both lasers were combined via a dichroic mirror (500 DRLP, Chroma Technology Corp., Rockingham Vermont, USA) and coupled into a single-mode optical fibre (cut-off $<$ 460 nm, NA 0.3, FC-APC/FC-PC, Schäfter+Kirchhoff, Hamburg, Germany) separating the emission module from the two other modules.

For the experiments proofing molecule internalisation, cell viability and long-lived observation low laser powers between 100 uW and 600 uW were used. The cell-based photobleaching studies were carried out using 3 mW (638 nm only) and the single-molecule tracks measurements were performed using high laser powers between 15 mW to 23 mW.

After the fibre output, the excitation light was collimated and via a dichroic mirror (dual-pass 545 nm/600 nm, Semrock, Rochester, New York, USA) directed on the TIRF objective (100x, oil immersion objective, NA 1.4, Olympus, Shinjuku, Tokyo, Japan). In TIRF mode, the excitation light was focused onto the cover slide under a critical angle allowing total internal reflection at the glass-water/cell suspension interface: TIRF-angle $> \sin^{-1}(\frac{n_{H_2O}}{n_{glass}}) \sim 63°$. Through the total internal reflection an evanescent electromagnetic field was generated penetrating about 100 nm deep in to the cell layer. In near-TIRF mode this TIRF-angle was decreased in such a way that laser light partially goes through the sample without total internal reflection allowing a deeper view into the sample. This method still uses the good signal-to-noise of the TIRF illumination (reduction of background fluorescence) by illuminating more of the sample. In wide-field mode the laser light was directly focused in the cell layer between cover slide and agarose pad. The cover slide was placed on a microscope stage which allowed the control of x/y/z movement of the cover slide relative to the

objective and supported the cover slide to reduce defocussing.

The emitted fluorescence signal from the sample was collected by the same microscope objective and separated from the excitation laser light by the dichroic mirror (dual-pass 545 nm/600 nm, Semrock, Rochester, New York, USA) and two emission filters (EmF1: 633/25 nm notch filter, Semrock and EmF2: 545 nm long-pass filter, Chroma). The green and red fluorescence emission channel were spectrally separated (630 nm dichroic long-pass filter, Omega, Vermont, USA) and focussed on two separate regions of an electron-multiplying charged-coupled device camera (EMCCD, Andor, iXon, Belfast, UK). The total magnification of the setup was 170x (94 nm x 94 nm per pixel).

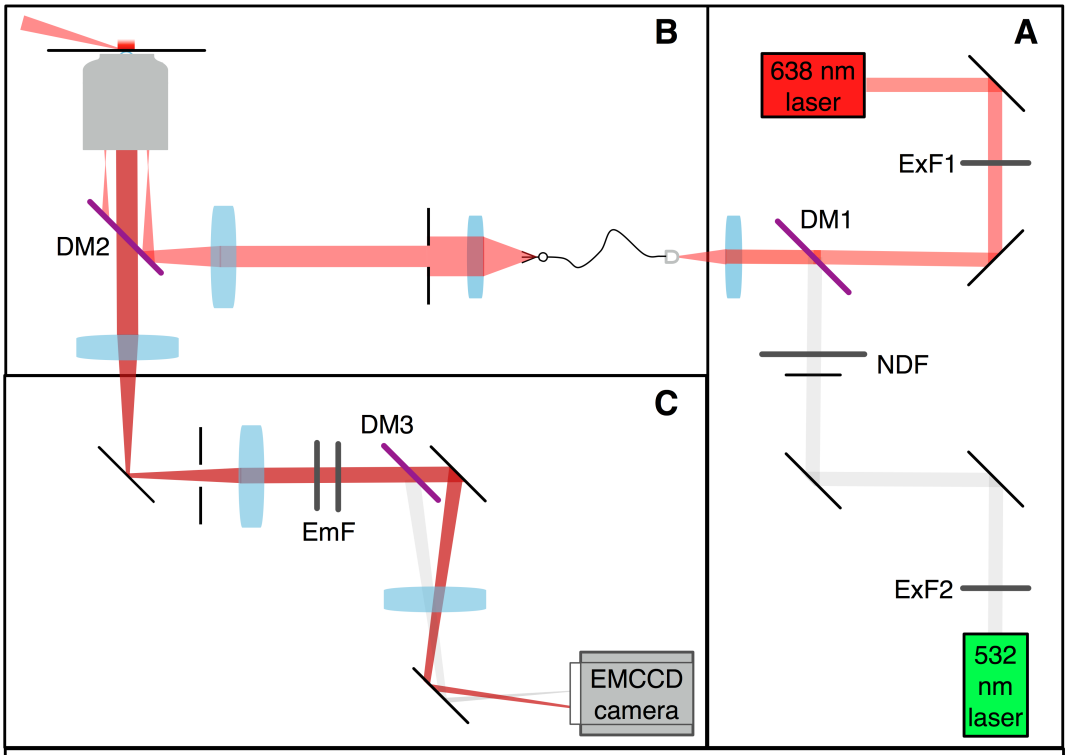

A. Excitation module ExF1 - excitation filter (640/10 bandpass), ExF2 - excitation filter (532/10 bandpass), DM1 - dichroic mirror (500 DRLP), NDF - neutral density filter wheel
B. Sample module DM2 - dichroic mirror (dual-pass 545/650)
C. Emission module EmF - emission filters (red laser notch filter 633/25, 545 long-pass), DM3 - dichroic mirror (630 DRLP)

Figure A.3: Schematic of inverted total internal reflection microscope setup with dual-colour detection.

A.4 Data analysis

A.4.1 Cell segmentation

Manual and trainable cell segmentation

Several segmentation attempts were pursuit to gain a fast cell segmentation tool for further cell fluorescence analysis.

Manual cell segmentation was implemented using a Matlab script where the user clicked around cell outlines in the white-light image, a mask of all cells was generated and used to extract the cells' fluorescent intensity from the raw fluorescence movies. This method worked fine but was very tedious and time consuming.

A more powerful idea was to use a trainable segmentation routine to learn the machine how *E.coli* cells look in the acquired white-light images. Here, I tested the Trainable Segmentation PlugIn in *fiji/ImageJ*[1] which recognises and segments pattern in electron microscope images (76). The algorithm was trained with about 20 white-light images by drawing image features in the white-light image and classifying the image components in categories such as cell membrane, cell cytoplasm or agarose pad/background. This training seemed already sufficient and a cell mask was generated by the trainable algorithm. The export of the cell mask from *fiji* to Matlab (or the further analysis of the fluorescence movies within *fiji*) was not pursued further.

Automated cell segmentation

For automated cell segmentation a program called 'Schnitzcells' developed by the Elowitz lab (63) and publicly available[2] was used. 'Schnitzcells' was developed for

[1] `http://fiji.sc/Trainable_Segmentation_Plugin`, 5/11/12, 12.15pm
[2] `http://cell.caltech.edu/schnitzcells/`, 5/11/12, 12.20pm

analysing gene expression using fluorescence time-lapse microscopy.

I adapted the automated cell segmentation and manual segmentation adjustment (scripts written in Matlab) that were implemented in the software (77). Since 'Schnitzcells' segmentation algorithm uses contrast detection and pattern (cell shape) recognition on phase-contrast cell images, I inverted the contrast of our white-light cell images and changed the cell shape parameters such as minimum cell area/length and maximum cell width in pixels according to the white-light images of our microscope setups (i.e. microscope magnification).

Using 'Schnitzcells', the cells were segmented in the white-light image automatically. Then the segmentation mask could be manually checked or corrected (deleting, adding, connecting, dividing cells) using a custom-friendly Matlab graphical user interface, fig. A.4. The adjusted cell mask was then used to extract the cells' fluorescence data such as initial cell intensities for internalisation efficiency studies or the cellular fluorescence over time for photobleaching analysis. The adaptation of the automated cell segmentation tool speeded up our data analysis and allowed us to gain good cell-based fluorescence statistics (300-500 cells per sample per day). This segmentation routine is superior to the previously developed segmentation scripts especially since it is less time consuming and already implemented into Matlab.

This segmentation method is strongly dependent on the contrast of the bright-field images. Segmentation works better when the bright-field images were taken with an LED white-light source with a narrower spectral range instead of a conventional white-light lamp source. To achieve the highest contrast between cells and background phase contrast microscopy has to be implemented. This is costly (new microscope objective needed) and requires new setup alignment.

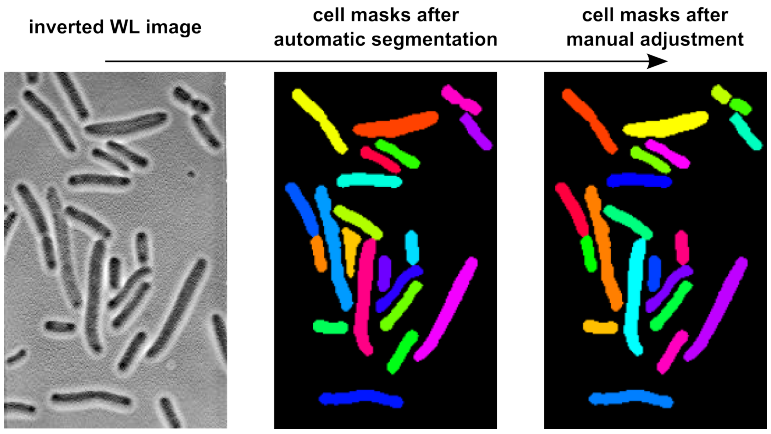

Figure A.4: Cell segmentation using Schnitzcells. An inverted white-light image is used as input for contrast detection and cell shape recognition using Schnitzcells, output cell mask. Left: inverted white-light image, Middle: Cell masks after automatic segmentation, Right: Cell masks after manual adjustment of segmentation. Different colours denote different segmented cells.

A.4.2 HMM photobleaching time trace analysis

We modelled the photobleaching time series as arising from a stochastic process where a finite sequence of random variables maps the underlying state sequence which assumes values in a discrete state space (of active fluorophores). Markov analysis proves suitable for our work as photobleaching time series should obey the Markov assumption: first-order state dependence. We describe an HMM via a parameter set $\lambda = (\pi, A, B)$.

- π, initial state distribution – π_i describes the probability of being in state i at time $t = 0$, where $1 \leq i \leq N$ and N is the maximum number of states
- A, state transition probabilities – A is a matrix that describes the probability a_{ij} of transitivity from state i to state j, $1 \leq i, j \leq N$
- B, observation probability distribution – B describes the probability $b_i(k)$ of observation k in state i

We can calculate the total observation probability by summing over all possible hidden state sequence probabilities. Baum and colleagues provided an efficient calculation of such a sum (78). The basic idea is to systematically vary the parameters to maximise the maximum likelihood. Such a likelihood results from obtaining the parameters maximum likelihood estimate (68, 69). To determine the "optimal" state sequence, we used the Viterbi algorithm (70, 71).

Hidden Markov Modelling has several drawbacks. First, model selection is not straight forward, i.e. the problem of determining the correct number of states. Second, the associated computational effort increases with N^2T where N is the number of states and T is the number of time points; thus, no real-time analysis is possible. Third, HMM performs best when the states can be clearly resolved and the states' lifetime are at least 10x greater than the sampling interval. Consequently, HMM has difficulty resolving short-lived states. Fourth, we need to accurately describe the initial probability distribution, otherwise the model may trap in local minima. Fifth, HMM analysis works best when each state is populated at least 10 times during a time series. In order to determine HMM appropriate and accuracy, researchers should always verify and validate HMM results with simulations, alternative analysis methods and experimental controls.

The algorithm used for analysis was adopted from (79) and implemented by Kristofer Gryte.

A.4.3 Single-molecule tracking and diffusion analysis

The used custom-written MATLAB software to analyse single-molecule tracking and diffusion in live E.coli was developed by Stephan Uphoff and is described in (72). A similar approach to analyse diffusion behaviour of single-molecules in bacterial cells was already presented by Manley et al. (80) and the Elf group (81, 60).

The single-molecule data analysis carried out in this work can be separated into four parts; the localisation of the single-molecule, the tracking of the molecule throughout the movie, the calculation of the mean-squared displacement – a measure of the molecules movement and obtaining an apparent diffusion coefficient distribution – a measure of the ensemble molecule movement. These four steps are illustrated in fig. A.5.

The image of a single fluorescent molecule on the camera chip is a diffraction-limited spot (point spread function – PSF) which is determined by the microscope setup properties (82). To determine the PSF positon (localising the molecule) an algorithm presented in (83, 75) was used. Briefly, the fluorescence image was band-pass filtered to minimise noise (high-pass filter) and reduce large-scale background (low-pass filter). For an initial position guess of the molecules a simple fixed intensity threshold was applied to the filtered fluorescence image of each movie frame. So detected PSFs were fitted by a 2D elliptical Gaussian

$$f(x,y) = A{\cdot}\exp\left(-\frac{((x-x_0)\cos\theta-(y-y_0)\sin\theta)^2}{2\sigma_x^2}-\frac{((x-x_0)\sin\theta+(y-y_0)\cos\theta)^2}{2\sigma_y^2}\right)+BG$$

with free fit parameters: x_0/y_0 position, σ_x/σ_y width, elliptical rotation angle θ, amplitude A, background BG. The number of emitted photons of a fluorophore within the exposure time is determined by the volume underneath the Gaussian curve. The background BG is fitted to account for background noise of the camera, the cellular autofluorescence and incomplete filtering of the excitation light.

Single-molecule tracking was performed by adapting the MATLAB script based on an algorithm described in (84). Localised PSFs were linked to a track if they appeared in consecutive frames within a window of 5 or 7 pixels (0.48 µm-0.67 µm) for exposure times of 10 ms and 15 ms, respectively. To account for disappearance of the PSF due to blinking or missed localisation, I used a memory parameter of 1 frame.

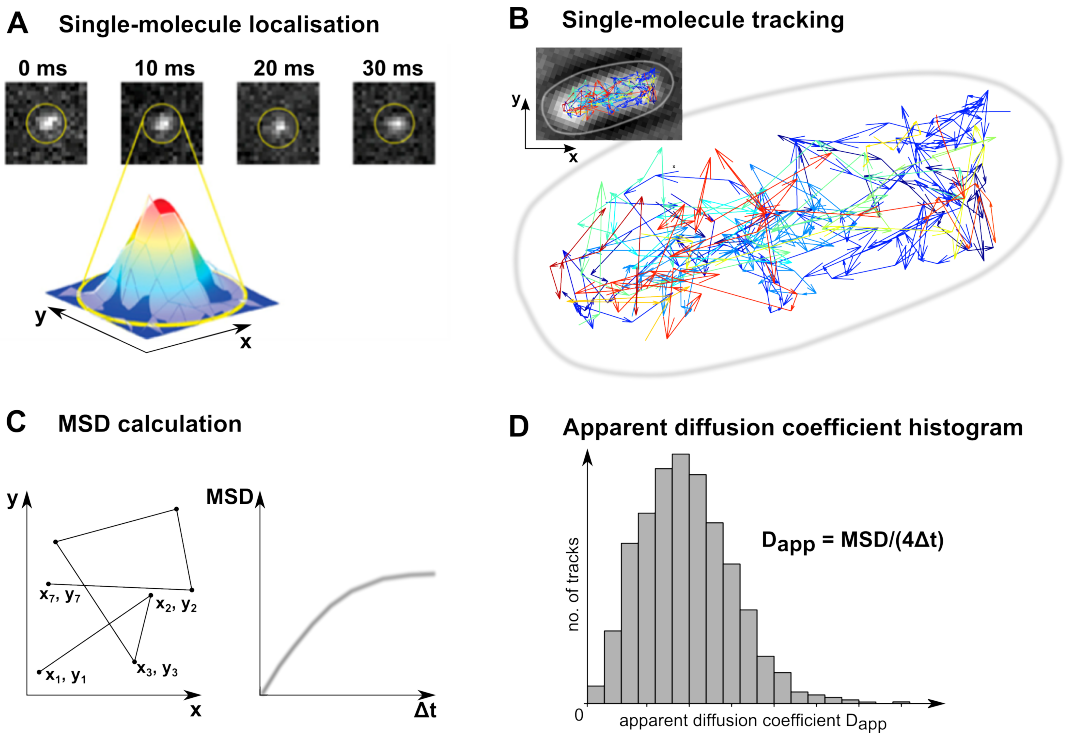

Figure A.5: Principle of single-molecule fluorescence analysis. **A.** Single-molecule localisation via fitting of a 2D Gaussian to the PSF. **B.** Tracking of single-molecules if they appeared in consecutive frame. **C.** Calculation of the mean-squared displacement (MSD) for each track. **D.** Calculation of the apparent diffusion coefficient from the MSD and analysis of the apparent diffusion coefficient distribution.

For each track with a minimum of 4 steps an apparent diffusion coefficient was calculated from the average of the mean squared displacements of each step, $D_{\text{app}} = \overline{\text{MSD}}/(4\Delta t)$ with Δt the frame time (= exposure time + frame read-out time from the camera chip). The apparent diffusion coefficients were plotted in a histogram where a peak at zero corresponds to non-diffusing molecules. We note that the apparent diffusion coefficient was corrected for the offset localisation standard deviation of 30 nm but does correspond to an accurate microscopic diffusion coefficient because of cell confinement and motion blurring (85). The diffusion analysis method was tested simulating 2D Brownian motion in a confined 'rod-shaped' area showing good agreement of experimental and simulated data (72).

The value for the localisation intensity threshold (crucial for PSF localisation) was

chosen in such a way that less than 5% of molecules were picked up in the negative control or the empty cell sample compared to the electroporated sample (rule of thumb). Furthermore, no tracks were observed in these controls since only tracks with more than 3 steps inside the cell boundary were taken for diffusion coefficient analysis. Inner cellular noise or non-internalised DNA outside the cell were picked up by the localisation algorithm but could not be linked (noise) or were excluded from the analysis (non-internalised DNA).

In this work, long-lived single-molecule tracks were visualised with a time dependent colour code within the cell outline. The photon count (integral of fitted PSF over background divided by the gain factor of $4.55\,\mathrm{counts/photon}$) of the tracked molecules were plotted throughout the track. Furthermore, the tracked molecules were plotted on top of the raw data and saved in a tif-movie file for visualisation of the single-molecule tracking.

Bibliography

[1] S Weiss. Fluorescence Spectroscopy of Single Biomolecules. *Science*, 283: 1676–1683, 1999.

[2] XS Xie, PJ Choi, GW Li, NK Lee, and G Lia. Single-Molecule Approach to Molecular Biology in Living Bacterial Cells. *Annual Review of Biophysics*, 37: 417–444, 2008.

[3] GW Li and XS Xie. Central dogma at the single-molecule level in living cells. *Nature*, 475:308–315, 2011.

[4] AN Kapanidis and T Strick. Biology, one molecule at a time. *Trends in Biochemical Science*, 34:234–243, 2009.

[5] J Elf, GW Li, and XS Xie. Probing Transcription Factor Dynamics at the Single-Molecule Level in a Living Cell. *Science*, 316:1191–1194, 2007.

[6] PJ Choi, L Cai, K Frida, and XS Xie. A stochastic single-molecule event triggers phenotype switching of a bacterial cell. *Science*, 322:442–446, 2008.

[7] EA Lipman, B Schuler, O Bakaijin, and WA Eaton. Single-Molecule Measurement of Protein Folding Kinetics. *Science*, 301:1233–1235, 2003.

[8] S Van de Linde, M Heilemann, and M Sauer. Live-Cell Super-Resolution Imaging with Synthetic Fluorophores. *Annual Review of Physical Chemistry*, 63:519–540, 2012.

[9] Y Santoso, CM Joyce, O Potapova, L Le Reste, J Hohlbein, JP Torella, ND Grindley, and AN Kapanidis. Conformational transitions in DNA polymerase I revealed by single-molecule FRET. *Proceedings of the National Academy of Sciences U S A*, 2:715–720, 2010.

[10] J Delch, EM Judd, HH McAdams, and WE Moerner. Visualization of the movement of single histidine kinase molecules in live *Caulobacter* cells. *Proceedings of the National Academy of Sciences U S A*, 101(45):15921–15926, 2004.

[11] J Yu, J Xiao, X Ren, K Lao, and XS Xie. Probing Gene Expression in Live Cells, One Protein Molecule at the Time. *Science*, 311:1600–1603, 2006.

[12] JJ Sakon and KR Weninger. Detecting the conformation of individual proteins in live cells. *Nature Methods*, 7(3):203–205, 2010.

[13] MJ Rust, M Bates, and X Zhuang. Sub-diffraction-limit imaging by stochastic optical reconstruction microscopy. *Nature Methods*, 3(10):793–795, 2006.

[14] EB Shera, NK Seitzinger, LM Davis, RA Keller, and SA Soper. Detection of single fluorescent molecules. *Chemical Physics Letters*, 174:553–557, 1990.

[15] JR Lakowicz. *Principles of Fluorescence Spectroscopy*. Springer-Verlag, 2006.

[16] M Sauer, J Hofkens, and J Enderlein. *Handbook of Fluorescence Spectroscopy and Imaging*. John Wiley & Sons, 2011.

[17] J Widengren, A Chmyrov, C Eggeling, PA Löfdahl, and CAM Seidel. Stategies to Improve Photostabilities in Ultrasensitive Fluorescence Spectroscopy. *Journal of Physical Chemistry*, 111:429–440, 2007.

[18] C Eggeling, J Widengren, R Rigler, and CAM Seidel. Photobleaching of Fluorescent Dyes under Conditions Used for Single-Moecule Detection: Evidence of Two-Step Photolysis. *Analytical Chemistry*, 70(13):2651–2659, 1998.

[19] RE Benesch and R Benesch. Enzymatic Removal of Oxygen for Polarography and Related Methods. *Science*, 118(3068):447–448, 1953.

[20] Y Harada, K Sakurada, T Aoki, DD Thomas, and T Yanagida. Mechanochemical coupling in actomyosin energy transduction studied by *in vitro* movement assay. *Journal of Molecular Biology*, 216:49–68, 1990.

[21] CE Aitken, RA Marshall, and JD Puglisi. An oxygen scavenging system for improvement of dye stability in single-molecule fluorescence experiments. *Biophysical Journal*, 94:1826–1835, 2008.

[22] T Ha and P Tinnefeld. Photophysics of Fluorescent Probes for Single-Molecule Biophysics and Super-Resolution Imaging. *Annual Review of Physical Chemistry*, 63:595–617, 2012.

[23] A Kishino and T Yanagida. Force measurements by micromanipulation of a single actin filament by glass needled. *Nature*, 334:74–76, 1988.

[24] M Heilemann, E Margeat, R Kasper, M Sauer, and P Tinnefeld. Carbocyanine Dyes as Efficient Reversible Single-Molecule Optical Switch. *Journal of the American Chemical Society*, 127(11):3801–3806, 2005.

[25] M Bates, TR Blosser, and X Zhuang. Short-Range Spectroscopic Ruler Based on a Single-Molecule Optical Switch. *Physical Review Letters*, 94(108101), 2005.

[26] I Rasnik, SA McKinney, and T Ha. Nonblinking and long-lasting single-molecule fluorescence imaging. *Nature Methods*, 3(11):891–893, 2006.

[27] J Vogelsang, R Kasper, C Steinhauer, B Person, M Heilemann, M Sauer, and P Tinnefeld. A Reducing and Oxidizing System Minimizes Photobleaching and Blinking of Fluorescent Dyes. *Angewandte Chemie International Edition*, 47 (108101):5465–5469, 2008.

[28] T Cordes, J Vogelsang, and P Tinnefeld. On the Mechanism of Trolox as Antiblinking and Antibleaching Reagent. *Journal of the American Chemical Society*, 131:5018–5019, 2008.

[29] SA Jones, SH Shim, J He, and X Zhuang. Fast, three-dimensional super-resolution imaging of live cells. *Nature Methods*, 75:499–505, 2011.

[30] K Xu, HP Babcock, and X Zhuang. Dual-objective STORM reveals three-dimensional filament organization in the actin cytoskeleton. *Nature Methods*, 9(2):186–188, 2012.

[31] M Cooper, A Ebner, M Briggs, M Burrows, N Gardner, R Richardson, and R West. Cy3B: improving the performance of cyanine dyes. *Journal of fluorescence*, 14(2):145–150, 2004.

[32] 11/11/2012, 11.05am. URL `http://www.atto-tec.com/attotecshop/product_info.php?language=en&info=p114_ATTO-674N.html`.

[33] 11/11/2012, 11.10am. URL `http://www.invitrogen.com/site/us/en/home/References/Molecular-Probes-The-Handbook/Technical-Notes-and-Product-Highlights/The-Alexa-Fluor-Dye-Series.html`.

[34] 11/11/2012, 11.20am. URL `http://www.invitrogen.com/site/us/en/home/References/Molecular-Probes-The-Handbook/tables/Fluorescence-quantum-yields-and-lifetimes-for-Alexa-Fluor-dyes.html`.

[35] RY Tsien. The Green Fluorescent Protein. *Annual Review of Biochemistry*, 67: 509–544, 1998.

[36] GS Baird, DA Zacharias, and RY Tsien. Biochemistry, mutagenesis, and oligomerization of DsRed, a red fluorescent protein from coral. *Proceedings of the National Academy of Sciences U S A*, 97(22):11984–11989, 2000.

[37] RM Dickson, AB Cubitt, RY Tsien, and WE Moerner. On/off blinking and switching behaviour of single molecules of green fluorescent protein. *Nature*, 388: 355–358, 1997.

[38] WE Moerner. Single-molecule optical spectroscopy of autofluorescent proteins. *Journal of Chemical Physics*, 117(24):10925–10937, 2002.

[39] K Kolmakov, VN Belov, J Bierwagen, C Ringemann, V Müller, C Eggeling, and SW Hell. Red-Emitting Rhodamine Dyes for Fluorescence Microscopy and Nanoscopy. *Chemistry – A European Journal*, 16:158–166, 2010.

[40] C Eggeling, R Ringemann, G Medda, G Schwarzmann, K Sandhoff, S Polyakova, VN Belov, B Hein, C von Middendorff, A Schönle, and SW Hell. Direct observation of the nanoscale dynamics of membrane lipids in a living cell. *Nature*, 457(7233):1159–1162, 2009.

[41] A Keppler, H Pick, C Arrivoli, H Vogel, and K Johnsson. Labeling of fusion proteins with synthetic fluorophores in live cells. *Proceedings of the National Academy of Sciences U S A*, 101(27):9955–9959, 2004.

[42] LW Miller, Y Cai, MP Sheetz, and VW Cornish. *In vivo* protein labeling with trimethoprim conjugates: a flexible chemical tag. *Nature Methods*, 2:255–257, 2005.

[43] SK Silverman. *In vitro* selection, characterization, and application of deoxyribozymes that cleave RNA. *Nucleic Acids Research*, 33(19):6151–6163, 2005.

[44] Y Sako, S Minoguchi, and T Yanagida. Single-molecule imaging of EGFR signaling on the surface of living cells. *Nature Cell Biology*, 2:168–172, 2000.

[45] JA Wyber, J Andrews, and A D'Emanuele. The Use of Sonification for the Efficient Delivery of Plasmid DNA into Cells. *Pharmaceutical Research*, 14(6): 750–756, 1997.

[46] T Kues, A Dickmanns, R Lührmann, R Peters, and U Kubitscheck. High interanuclear mobility and dynamic clustering of the splicing factor U1 snRNP observed by single particle tracking. *Proceedings of the National Academy of Sciences U S A*, 98(21):12021–12026, 2001.

[47] JP Knemeyer, DP Herten, and M Sauer. Detection and Identification of Single Molecules in Living Cells Using Spectrally Resolved Fluorescence Lifetime Imaging Microscopy. *Analytical Chemistry*, 75(9):2147–2153, 2003.

[48] H Murakoshi, R Iino, T Kobayashi, T Fujiwara, C Ohshima, A Yoshimura, and A Kusumi. Single-molecule imaging analysis of Ras activation in living cells. *Proceedings of the National Academy of Sciences U S A*, 101(19):7317–7322, 2004.

[49] JC Weaver and YA Chizmadzhev. Theory of electroporation: A review. *Bioelectrochemistry and Bioenergetics*, 41(2):135–160, 1996.

[50] E Neumann, M Schäfer-Ridder, Y Wang, and PH Hofschneider. Gene transfer into mouse lyoma cells by electroporation in high electric fields. *The European Molecular Biology Organization Journal*, 1(7):841–845, 1982.

[51] H Potter, L Weir, and P Leder. Enhancer-dependent expression of human kappa immunoglobulin genes introduced into mouse pre-B lymphocytes by electroporation. *Proceedings of the National Academy of Sciences U S A*, 81:7161–7165, 1984.

[52] M Hibino, M Shigemori, K Itoh, K Nagayama, and K Kinosita. Membrane conductance of an electroporated cell analyzed by submicrosecond imaging of transmembrane potential. *Biophysical Journal*, 59(1):209–220, 1991.

[53] WJ Dower, JF Miller, and CW Ragsdale. High-efficiency transformation of *e.coli* by high-voltage electroporation. *Nucleic Acids Research*, 16:6127–6145, 1988.

[54] J Popp, VV Tuchin, A Chiou, and SH Heinemann. *Handbook of Biophotonics*. John Wiley & Sons, 2011.

[55] B Alberts, A Johnson, J Lewis, M Raff, K Roberts, and P Walter. *Molecular Biology of the Cell 5E*. Garland Science, 2008.

[56] FR Blattner, G Plunkett III, CA Bloch, NT Perna, V Burland, M Riley, J Collado-Vides, JD Glasner, CK Rode, GF Mayhew, J Gregor, NW Davis, HA Kirkpatrick, MA Goeden, DJ Rose, B Mau, and Y Shao. The Complete Genome Sequence of *Escherichia coli* K-12. *Science*, 277(5331):1453–1462, 1997.

[57] Y Sowa, AD Rowe, MC Leake, T Yakushi, M Homma, A Ishijima, and RM Berry. Direct observation of steps in rotation of the bacterial flagellar motor. *Nature*, 437:916–919, 2005.

[58] T Pilizota, Y Sowa, and RM Berry. Rotary proteins. *in Handbook of Single-molecule Biophysics, Chapter 7, Springer*, Ed. P Hinterdorfer, A van Oijen, 2009.

[59] IA Berlatzky, A Rouvinski, and S Ben-Yehuda. Spatial organization of a replicating bacterial chromosome. *Proceedings of the National Academy of Sciences U S A*, 105(37):14136–14140, 2008.

[60] P Hammar, P Leroy, A Mahmutovic, EG Marklund, OG Berg, and J Elf. The *lac* Repressor Displays Facilitated Diffusion in Living Cells. *Science*, 336:1595–1598, 2012.

[61] M Tokunaga, N Imamoto, and K Sakata-Sogawa. Highly inclined thin illumination enables clear single-molecule imaging cells. *Nature Methods*, 5(2):159–161, 2008.

[62] R Crawford*, JP Torella*, L Aigrain*, **A Plochowietz***, K Gryte, S Uphoff, and AN Kapanidis. Long-lived, ultrasensitive intracellular fluorescence using electroporated biomolecules. in preparation, designated for *Nature Methods*, *equal contribution, Nov 2012.

[63] JW Young, JCW Locke, A Altinok, N Rosenfeld, T Bacarian, PS Swain, E Mjolsness, and MB Elowitz. Measuring single-cell gene expression dynamics in bacteria using fluorescence time-lapse microscopy. *Nature Protocols*, 7(1):80–88, 2012.

[64] MC Leake, JH Chandler, GH Wadhams, F Bai, RM Berry, and JP Armitage. Stoichiometry and turnover in single, functioning membrane protein complexes. *Nature*, 443:355–358, 2006.

[65] T Lenn, CN Gkekas, L Bernard, C Engl, G Jovanovic, M Buck, and L Ying. Measuring the stoichiometry of functional PspA complexes in living bacterial cells by single molecule photobleaching. *Chemical Communications*, 47:400–402, 2011.

[66] SH Chung and RA Kennedy. Forward-backward non-linear filtering technique for extracting small biological signals from noise. *Journal of Neuroscience Methods*, 40(1):71–86, 1991.

[67] TC Messina, H Kim, JT Giurleo, and DS Talaga. Hidden Markov Model Analysis of Multichromophore Photobleaching. *Journal of Physical Chemistry B*, 110(33): 16366–16376, 2006.

[68] LE Baum and T Petrie. Statistical inference for probabilistic functions of finite state Markov chains. *The Annals of Mathematical Statistics*, 37(6):1554–1563, 1966.

[69] LE Baum, T Petrie, G Soules, and N Weiss. A maximization technique occurring in the statistical analysis of probabilistic functions of Markov chains. *The Annals of Mathematical Statistics*, 41(1):164–171, 1970.

[70] G Forney. The viterbi algorithm. *Proceedings of the IEEE*, 61(3):268–278, 1973.

[71] A Viterbi. Error bounds for convolutional codes and an asymptotically optimum decoding algorithm. *IEEE Transactions on Information Theory*, 13(2):260–269, 1967.

[72] S Uphoff, R Reyes-Lamothe, F Garza de Leon, DJ Sherrat, and AN Kapanidis. Single-molecule DNA repair in live bacteria. Nov 2012.

[73] Y Kim, SH Eom, J Wang, DS Lee, SW Suh, and TA Steitz. Crystal structure of Thermus aquaticus DNA polymerase. *Nature*, 376(6541):612–616, 1995.

[74] PH Patel, M Suzuki, E Adman, A Shinkai, and LA Loeb. Prokaryotic DNA polymerase I: evolution, structure and ”base flipping” mechanism for nucleotide selection. *Journal of Molecular Biology*, 308(5):823–837, 2001.

[75] SJ Holden, S Uphoff, and AN Kapanidis. DAOSTORM: an algorithm for high-density super-resolution. *Nature Methods*, 8(4):279–280, 2011.

[76] 18/10/2012, 12.05pm. URL `http://fiji.sc/wiki/index.php/Trainable_Segmentation_Plugin_Implementation`.

[77] Elowitz lab. Schnitzcells User's Manual – Software for Quantitative Analysis of Time-Lapse Movies. *Release*, 1.1, June 01, 2011.

[78] LE Baum and JA Eagon. An inequality with applications to statistical estimation for probabilistic functions of Markov processes and to a model for ecology. *Bulletin of the American Mathematical Society*, 73(3):360–363, 1967.

[79] Rabiner LR. A Tutorial on Hidden Markov Models and Selected Applications in Speech Recognition. *Proceedings of the IEEE*, 77(2):257–286, 1989.

[80] S Manley, JM Gillette, GH Patterson, H Shroff, HF Hess, E Betzig, and J Lippincott-Schwartz. High-density mapping of single-molecule trajectories with photoactivated localization microscopy. *Nature Methods*, 5:155–157, 2008.

[81] BP English, V Hauryliuk, A Sanamrad, S Tankov, NH Dekker, and J Elf. Single-molecule investigations of the stringent response machinery in living bacterial cells. *Proceedings of the National Academy of Sciences U S A*, 108(31):E365–E373, 2011.

[82] E Abbe. Beiträge zur Theorie des Mikroskops und der mikroskopischen Wahrnehmung. *M. Schultze's Archiv für mikroskopische Anatomie*, 9:413–468, 1873.

[83] SJ Holden, S Uphoff, J Hohlbein, D Yadin, Ludovic Le Reste, OJ Britton, and AN Kapanidis. Defining the Limits of Single-Molecule FRET Resolution in TIRF Microscopy. *Biophysical Journal*, 99:3102–3111, 2010.

[84] JC Crocker and DG Grier. Methods of Digital Video Microscopy for Colloidal Studies. *Journal of Colloid and Interface Science*, 179(1):298–310, 1996.

[85] X Michalet and AJ Berglund. Optimal diffusion coefficient estimation in single-particle tracking. *Physical Review E*, 85:061916, 2012.